Swiss J Geosci (2015) 108:55–74
DOI 10.1007/s00015-015-0178-z

Age of cleft monazites in the eastern Tauern Window: constraints on crystallization conditions of hydrothermal monazite

Edwin Gnos · Emilie Janots · Alfons Berger · Martin Whitehouse · Franz Walter · Thomas Pettke · Christian Bergemann

Received: 2 September 2014 / Accepted: 16 February 2015 / Published online: 13 March 2015

Abstract Monazite-bearing Alpine clefts located in the Sonnblick region of the eastern Tauern Window, Austria, are oriented perpendicular to the foliation and lineation. Ion probe (SIMS) Th–Pb and U–Pb dating of four cleft monazites yields crystallization ages of different growth domains and aggregate regions ranging from 18.99 ± 0.51 to 15.00 ± 0.51 Ma. The crystallization ages obtained are overlapping or slightly younger than zircon fission track ages but older than zircon (U–Th)/He cooling ages from the same area. This constrains cleft monazite crystallization in this area to ~300–200 °C. LA-ICP-MS data of dated hydrothermal monazites indicate that in graphite-bearing, reduced host lithologies, cleft monazite is poor in As and has higher La/Yb values and U concentrations, whereas in oxidised host rocks opposite trends are observed. Monazites show negative Eu anomalies and variable La/Yb values ranging from 520 to 6050. The positive correlation between Ca and Sr concentration indicates dissolution of plagioclase or carbonates as the source of these elements. The data show that early exhumation and cleft formation in the Tauern is related to metamorphic dome formation caused by the collision of the Adriatic with the European plate and that monazite crystallization in the clefts occurred later. Our data also demonstrate that hydrothermal monazite ages offer great potential in helping to constrain the chronology of exhumation in collisional orogens.

Keywords Monazite crystallization age · Alps · Hydrothermal activity · Retrograde metamorphism · Tectonic exhumation · Tauern Window · Austria

Editorial handling: A. G. Milnes.

E. Gnos (✉)
Natural History Museum Geneva, 1 Route de Malagnou, 1208 Geneva, Switzerland
e-mail: edwin.gnos@ville-ge.ch

E. Janots
ISTerre, 1381 Rue de la Piscine, 38041 Grenoble, France

A. Berger · T. Pettke
Institut für Geologie, Baltzerstrasse 1 + 3, 3012 Bern, Switzerland

M. Whitehouse
Swedish Museum of Natural History, Box 50007, 104-05 Stockholm, Sweden

F. Walter
Institut für Erdwissenschaften, Karl-Franzens-Universität, Universitätsplatz 2, 8010 Graz, Austria

C. Bergemann
Earth and Environmental Sciences, University of Geneva, Rue de Maraichers 13, 1205 Geneva, Switzerland

1 Introduction

Monazite, (LREE,Th,U)PO_4 represents an excellent mineral for combined $^{232}Th/^{208}Pb$, $^{238}U/^{206}Pb$ and $^{235}U/^{207}Pb$ isotopic dating of geologic processes (e.g., Parrish 1990). Monazite is very resistant to radiation damage (e.g., Meldrum et al. 1998, 1999, 2000; Nasdala et al. 1999), and U–Th-Pb resetting by solid diffusion is negligible (Cherniak et al. 2004). The numerous studies reporting monazite age "resetting" attribute it to dissolution-precipitation processes in the presence of fluids along with a modification of the chemical composition of the monazite (e.g., Seydoux-Guillaume et al. 2002; Hetherington et al. 2010; Harlov et al. 2011; Williams et al. 2011; Janots et al. 2012; Didier et al. 2013).

Monazite ages can be determined from Th-U–Pb concentrations (e.g., Suzuki and Adachi 1991; Suzuki et al.

1994; Montel et al. 1994, 1996; Scherrer et al. 2000). This assumes that the monazite has not incorporated common Pb and that the common Pb has a negligible influence on the age determination. This dating approach is especially useful in polymetamorphic regions, where rock-forming monazite generally shows complex, small-scale growth zoning (e.g., Berger et al. 2006; Krenn et al. 2011a; Schulz and von Raumer 2011). These can be dated only with the high spatial resolution provided by electron microprobe analysis (EMPA), unless the monazites are less than 100 Ma old such that EMPA is insufficient to precisely analyze the amount of Pb (e.g., Montel et al. 1996). Furthermore, initial/common Pb becomes important in young monazite, especially in hydrothermal environments (Krenn et al. 2011b; Seydoux-Guillaume et al. 2012).

Rare hydrothermal cleft monazite is commonly mm-sized in contrast to monazite from metamorphic rocks, which is normally <100 μm. Hydrothermal monazite growth patterns can display both dissolution and growth stages (Janots et al. 2012). Individual growth domains, identifiable by trace element variations (REE + Y, Th, U and Pb), are sufficiently large enough to be dated precisely utilizing in situ isotopic techniques (secondary ion mass spectrometry, SIMS, and inductively coupled plasma mass spectrometry, ICP–MS). In ideal cases it is even possible to resolve growth duration (Janots et al. 2012; Berger et al. 2013).

Alpine clefts formed in the presence of fluid at the ductile–brittle transition during or after the peak of metamorphism (e.g., Mullis et al. 1994; Mullis 1996). They represent open, originally fluid-filled voids in veins and fissures. They form during tectonic activity and are oriented roughly perpendicular to the lineation and foliation. Due to interaction of hot fluid (<500 °C) with the wall rock, dissolution of minerals occurs in the wall rock leading to the formation of porosity and an alteration halo around the cleft. New minerals precipitate in the open cleft space and in the wall rock pores. For this reason, many clefts display hydrothermal bleaching (dissolution of mafic minerals from the adjacent rock walls). The cleft mineralization does not represent a metamorphic paragenesis but a crystallization sequence that has grown during continuous fluid-rock interaction and dissolution and reprecipitation stages in response totectonic movements, exhumation, and cooling. This results in growth domains observed in the cleft monazite (e.g., Janots et al. 2012) and other cleft minerals.

Although micas and feldspars are frequent in alpine fissures, attempts to use them for dating crystallization in Alpine clefts have failed, in many cases, due to excess Ar accumulating in these minerals (e.g., Purdy and Stalder 1973).

Alpine clefts in some metasediments and metagranitoids (Niggli et al. 1940; Mannucci et al. 1986) have long been known to occasionally contain well-developed monazite crystals but only recently have dating attempts proved to be successful (Gasquet et al. 2010; Janots et al. 2012; Berger et al. 2013). The first successful cleft monazite study in the Lauzière massif, Western Alps (Gasquet et al. 2010), yielded two groups of $^{232}Th/^{208}Pb$ ages at 5–7 and 10–11 Ma, obtained by laser ablation inductively coupled plasma mass spectrometry (LA–ICP–MS). Corresponding $^{235}U/^{207}Pb$ ages were considered imprecise (low ^{207}Pb) and $^{238}U/^{206}Pb$ ages meaningless due to $^{206}Pb_{excess}$ (Gasquet et al. 2010). By using a SIMS, Janots et al. (2012) showed that hydrothermal monazite generally provides the most reliable dates with $^{232}Th/^{208}Pb$ dating due to $^{206}Pb_{excess}$ and the low radiogenic Pb component in the U–Pb system. Janots et al. (2012) also showed that $^{206}Pb_{excess}$ (due to isotopic disequilibrium in the ^{238}U-^{206}Pb decay chain) can reach 70 % of the total measured ^{206}Pb.

In combination with textural information, Janots et al. (2012) were able to show that two cleft monazites in the Gotthard and Aar Massifs, Switzerland, started to crystallize at 15.2 ± 0.3 and 14.1 ± 0.3 Ma, respectively. The youngest rims were dated at 13.5 ± 0.4 Ma. Monazites occurring in shear zones from the southern Aar Massif, yielded crystallization stages between 8.03 ± 0.22 Ma and 6.25 ± 0.60 Ma (Berger et al. 2013). The resolvable age difference shows that in both studies growth was episodic and lasted for 1–2 Ma. Moreover, in the Aar and Gotthard Massifs, monazite crystallization occurred a few million years after the cleft formation (Janots et al. 2012).

In this study we will present the crystallization ages of cleft monazites from the eastern Tauern window. We will show that the chemical and isotopic composition of monazite is influenced by the host rock composition that cleft formation is linked to Miocene metamorphic doming and that monazite crystallisation occurred later during exhumation.

2 Tectonic setting

2.1 Alpine context

In the Eastern Alps, Austroalpine nappes, derived from the Adriatic plate, predominate and overlie the Penninic and Subpenninic nappe stack (Fig. 1). This entire nappe stack has been affected by large-scale E-W oriented extension and doming in Early to Middle Miocene triggering unroofing of tectonically lower, Penninic and Sub-Penninic nappes (Fig. 1). These units are now exposed in the Tauern tectonic window (e.g., Schmid et al. 2004). In the Tauern Window (Fig. 1), Penninic crystalline basement nappes with Mesozoic sedimentary cover and structurally lower European plate units, including part of the distal deposits

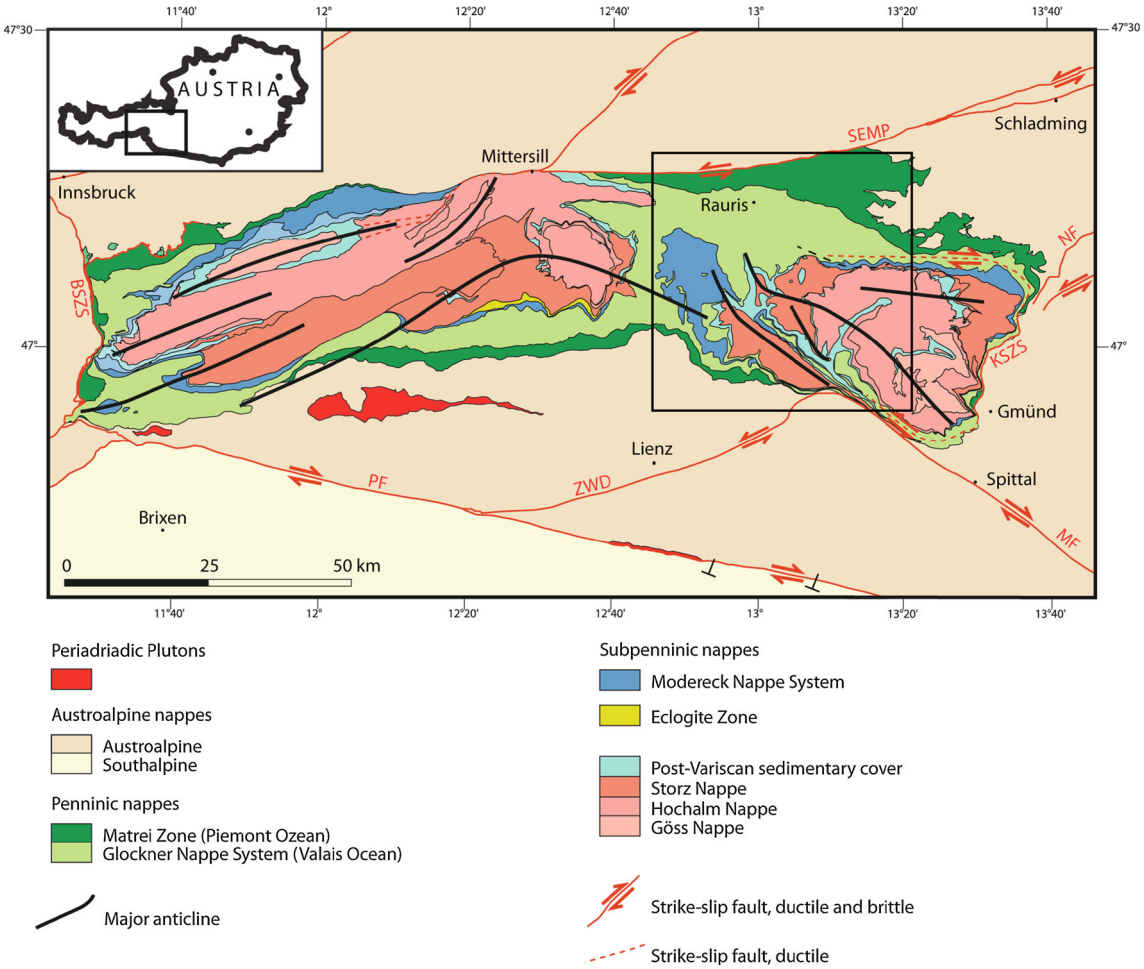

Fig. 1 Tectonic map of the Tauern Window according to Schmid et al. (2013). See *inset* for location. The tectonic window consists of a metamorphic dome forming the core of large anticlines produced during collision of the Europen and Adriatic plates. The formation is coeval with orogen-parallel extension (e.g. Ratschbacher et al. 1991; Frisch et al. 2000). Several Tertiary plutons occur in the region of the right-lateral Periadriatic line. *BSZS* Brenner shear zone system, *KSZS* Katschberg shear zone system, *MF* Mölltal Fault, *NF* Niedere Tauern Fault, *PF* Pustertal Fault, *SEMP* Salzach-Ennstal-Mariazell-Puchberg Fault, *ZWD* Zwischenbergen-Wöllatratten-Drau Fault

(Valaisan basin), occupy the core of the window. Both the Tauern and Rechnitz Penninic windows reached amphibolite facies metamorphism during the Alpine orogeny. The PT peak of this Barrovian metamorphism is dated at ~30 Ma in the Tauern Window (e.g., von Blanckenburg et al. 1989; Christensen et al. 1994; Inger and Cliff 1994). The metamorphic ages are thus younger than metamorphism in all other parts of the Eastern Alps (e.g., Hoinkes et al. 1999), but comparable to ages (e.g., Hunziker et al. 1992) obtained in the Lepontine metamorphic dome (Todd and Engi 1997).

2.2 Exhumation and cooling of the Tauern Window

Peak metamorphic conditions of up to 650 °C were reached in the structurally deepest units of the Tauern metamorphic dome by the end of the early Oligocene (Thöni 1999). This was in response to the Late Eocene to Early Oligocene collision of the European with the Adriatic continental plate that causes nappe stacking (Schmid et al. 2013 and references therein). Peak metamorphic temperatures reached ~500 °C in the Sonnblick area (Figs. 1, 2). Post-nappe folding (Hoinkes et al. 1999; Scharf et al. 2013; Figs. 1, 2) is related to N–S shortening and associated E-W oriented extension dated at 17.5–16.5 Ma (Steininger et al. 1996). These ages correspond to mica and zircon fission track data obtained in the eastern part of the Tauern Window (Dunkl et al. 2003; Scharf et al. 2013). Around 13 Ma this extensional phase and the rapid exhumation of Tauern Window rocks was terminated (Steininger et al. 1996).

Luth and Willingshofer (2008) and Rosenberg and Berger (2009) compiled age data providing information about post-collisional cooling of the Eastern Alps and

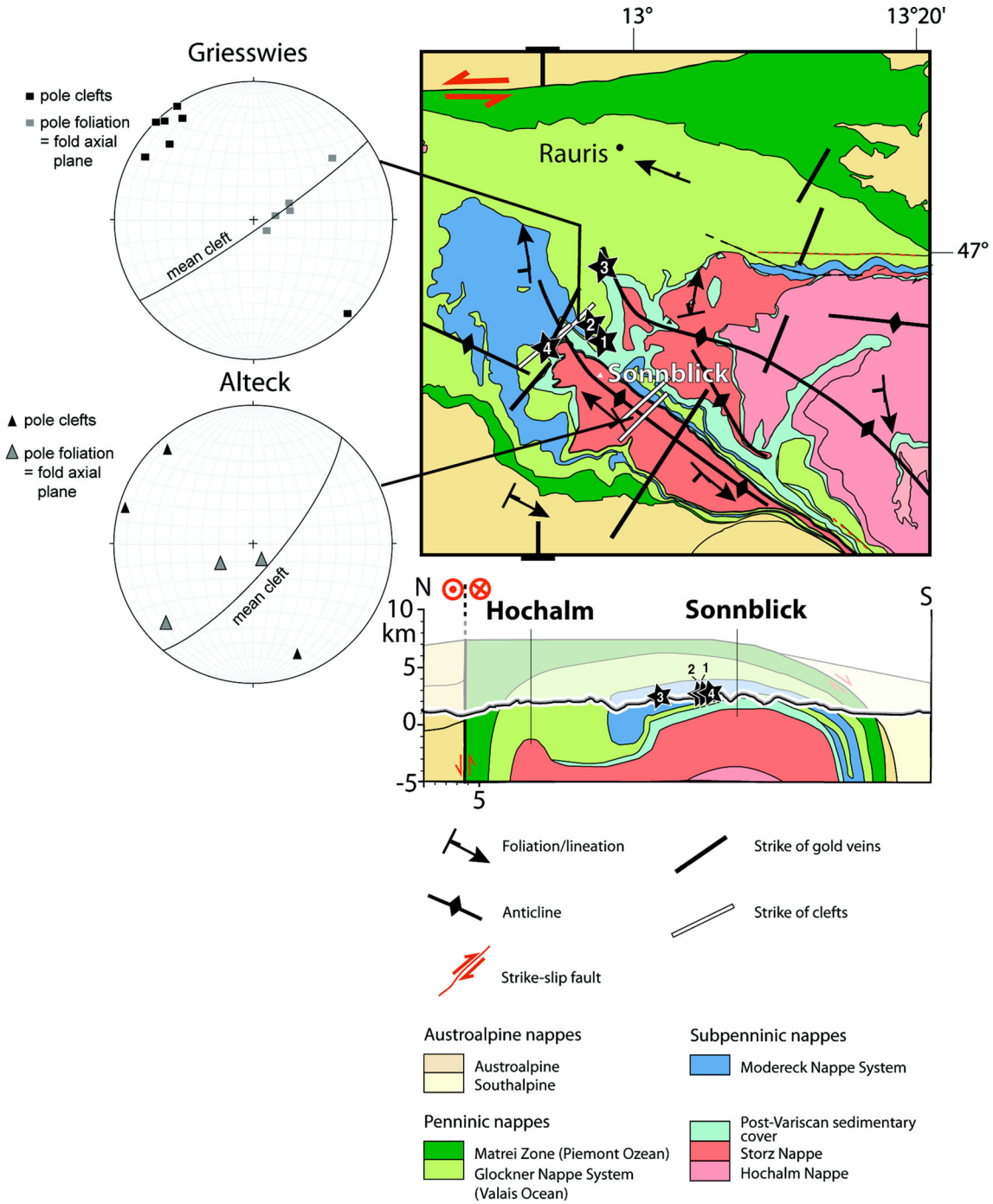

Fig. 2 Tectonic map of the eastern Tauern Window based on Scharf et al. (2013) and Schmid et al. (2013). Structural data are from Exner (1962) and gold vein information from Feitzinger and Paar (1991). Cleft and gold vein orientations mark trends. The length of the signs has no meaning. Numbered stars mark localities of dated cleft monazites (see Table 1): *1* Erfurter Steig; *2* Griesswies; *3* Lohninger Quarry; *4* Gjaidtroghöhe. Cross section, adapted from Schmid et al. (2013), shows sample localities in their tectonic position. The nappe parts shown above the *line* of the present topography indicate the amount of material eroded. TAUERN3 is placed at the locality from where the landslide material was derived. For lithology see Fig. 1

analysed the cooling pattern and the cooling rates of the Tauern Window. Their compilation showed that the eastern Tauern Window had cooled below the zircon fission track closure temperature of ca. 280–240 °C (Yamada et al. 1995; Bernet and Garver 2005; Reiners 2005; Bernet 2009) between 19 and 16 Ma (Dunkl et al. 2003; Foeken et al. 2007; Wölfler et al. 2012). Apatite fission track data show that the bulk of the Tauern Window had not cooled below

Table 1 Locations of the four analyzed Tauern cleft monazites

Locality	Sample	Latitude (°)	Longitude (°)	Altitude (m)	Rock	Crystallization Sequence
Erfurter Steig, Rauris, Salzburg	TAUERN1	47°04′06″	12°57′45″	2150	Bt-Mu schist (Schwarzschiefer)	Qtz, Alb, Adl, phenakite, Rt, Mnz, Cc,
Griesswies, Rauris, Salzburg	TAUERN2	47°04′26″	12°57′17″	2650	Bt-Mu schist (Schwarzschiefer)	Alb, Py, Qtz, Rt, Chl, euclase, Mnz, Xnt, goethite-todorokite-nordstrandite
Lohninger Quarry, Rauris, Salzburg	TAUERN3	47°07′47″	12°58′47″	1160	Meta-arenite	Alb, Qtz, Trm, Hem, Rt, Mnz
Gjaidtroghöhe, Grosses Fleisstal, Kärnten	TAUERN4	47°04′04″	12°54′30″	~2500	Gneiss	Qtz, Alb, anatase/Rt,Chl, Mnz, Cc

Adl adularia, *Rt* rutile and anatase, TiO_2, *Chl* clinochlore, euclase, $BeAlSiO_4(OH)$, goethite, FeO(OH), nordstrandite, $Al(OH)_3$, phenakite, Be_2SiO_4, todorokite, $(Na,Ca,K,Ba,Sr)_{1-x}(Mn,Mg,Al)_6O_{12}{\cdot}3\text{-}4H_2O$, *Trm* tourmaline, *Xnt* xenotime

~110 °C before 15 Ma (Staufenberg 1987; Foeken et al. 2007; Wölfler 2008), in contrast to the older cooling ages in Austroalpine units surrounding the study area (e.g., Hejl 1998; Dunkl et al. 2003; Wölfler et al. 2012).

3 Materials and methods

3.1 Sample locations and description

The monazite grains in this study were sampled by crystal searchers from steeply dipping, roughly NE-SW striking clefts located in the Sonnblick region of the eastern Tauern Window, Austria (Figs. 2, 3a, b). Only in the Erfurter Steig and Griesswies cases (Table 1) it was possible to visit the exploited mineral cleft. The other two clefts were quarried away or not accessible. Cleft monazite is rarely recognised in the field, because samples are generally covered by dirt. The monazites are from clefts hosted in metasedimentary rocks of the Modereck and Glockner nappe systems (Fig. 1; Schmid et al. 2013) that also occupy a synclinal position between the Sonnblick and Hochalm sub-domes (Fig. 2). The clefts (Fig. 3a, b) characteristically occur at the lower end of subvertical quartz veins located in lower amphibolite facies metamorphic metasedimentary gneisses and schists. The clefts are subvertical and oriented perpendicular to the main foliation and lineation (Fig. 2). Their orientation is at a small angle to the Au-bearing veins in the area (Feitzinger and Paar 1991; Fig. 2).

Monazites from the clefts (Fig. 3c, d) are yellow, brownish-yellow to rose in colour. They occur either as a crust consisting of 50–100 μm-sized crystals (Fig. 3c) or well-developed mm-sized individuals (Fig. 3d). Monazite is associated with albite (pericline), quartz, anatase/rutile, adularia, muscovite-phengite, carbonate, sulphides, chlorite, and rarely with hematite, tourmaline and the Be minerals euclase, $BeAlSiO_4(OH)$, and phenakite, Be_2SiO_4 (Table 1). Orthoclase (adularia), quartz, and albite-oligoclase ("pericline") were the first minerals to grow in the cleft. Monazite grew late on quartz, feldspar, euclase (Fig. 3c) and tourmaline (Fig. 3d), and is commonly coeval with rutile or anatase. In general, only clinochlore crystallised later than monazite (e.g., Niedermayr 1980).

Monazite TAUERN1 (star 1 in Fig. 2) is a crystal sitting on cleft quartz from the Erfurter Steig, Rauris, Salzburg (Fig. 3d). Monazite TAUERN2 (Fig. 2) forms a rose-coloured crust consisting of 50-100 μm-sized crystals in a cleft of the Griesswies, Rauris, Salzburg, where it occurs in association with albite and euclase (Table 1; Fig. 3c). Monazite TAUERN3 (Fig. 2) is a sample from the Lohninger quarry, Rauris, Salzburg, where gneiss blocks from the Permo-Triassic Wustkogel Formation (Frasl 1958) are quarried from pre-historic landslide material that originated from the western slope of the valley (Pestal et al. 2009). Monazite TAUERN4 (Fig. 2) is from the Gjaidtroghöhe, Grosses Fleisstal (Carintia). Monazite crusts and well-developed samples have been selected in order to test if their crystallization age is different.

3.2 Analytical techniques

Backscatter electron (BSE) images were obtained on a JEOL JXA8200 electron microprobe (EMPA) at the University of Copenhagen.

Th-U–Pb isotope analyses of monazite were obtained on a Cameca IMS1280 SIMS instrument at the Nordsims facility (Swedish Museum of Natural History). Analytical methods closely follow those described by Harrison et al. (1995) and Kirkland et al. (2009), using a −13 kV O_2^- primary beam of ~6 nA and nominal 15 μm diameter. The mass spectrometer was operated at +10 kV and a mass resolution of ca. 4300 (M/ΔM, at 10 % peak height) with data collected in peak hopping mode using an ion-counting electron multiplier. U–Pb and Th–Pb data were calibrated against an in-house reference monazite, C83-32 (Corfu

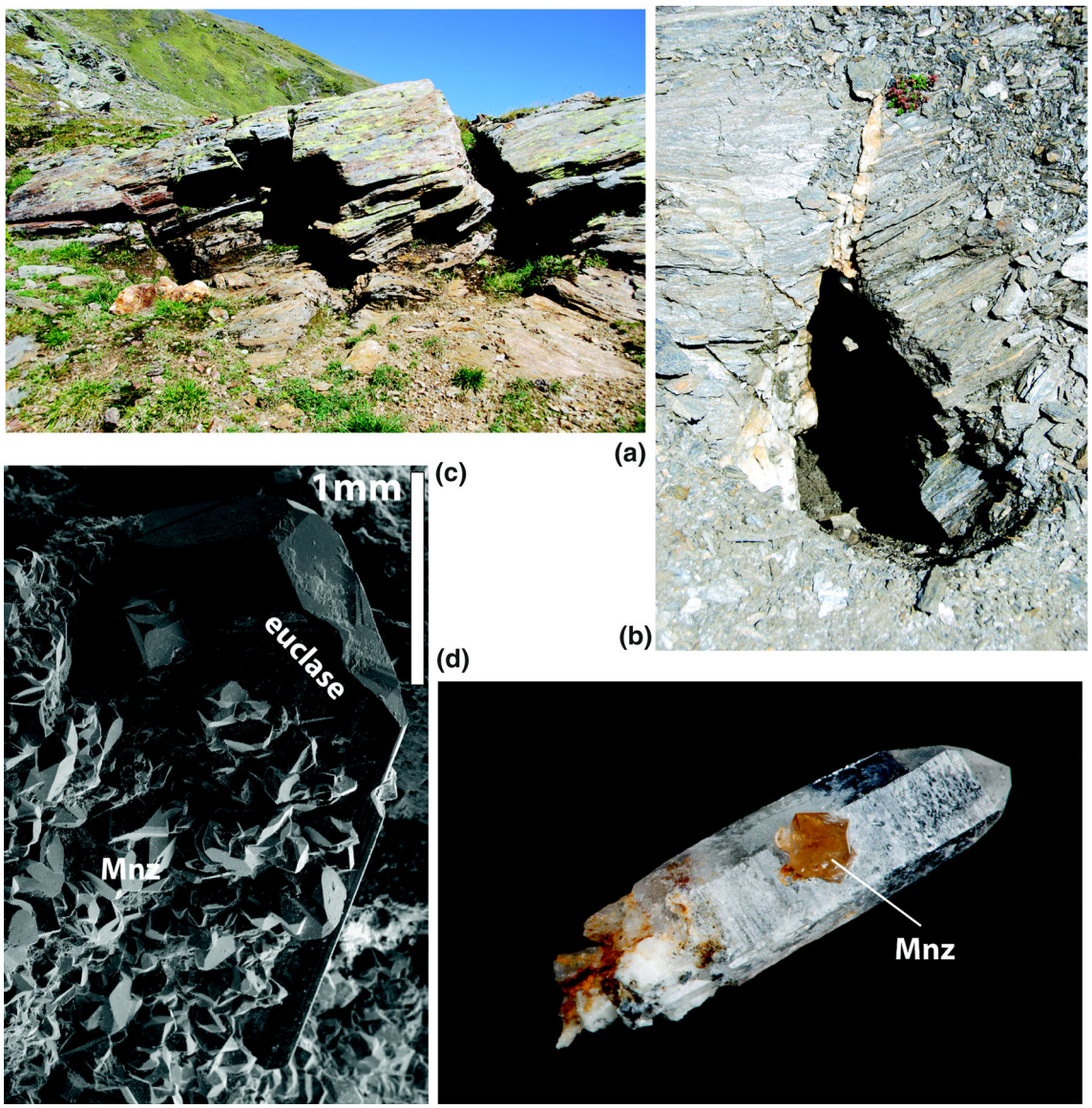

Fig. 3 Mineral clefts and monazites. **a** Series of parallel clefts in a 10 m sized outcrop of two-mica schist from the Griesswies, Rauris Valley. Their orientation is perpendicular to the foliation and lineation. **b** Quartz vein at Griesswies, Rauris Valley, showing the beginning of the rotation of the quartz vein into the foliation resulting in an oblique orientation relative to the foliation and lineation. Younger set of fractures is oriented perpendicular to the foliation and the lineation, which limits the exploited cleft room located at the lower end of the quartz vein. Image width is 2 m. **c** Secondary electron image showing TAUERN2 monazite crystals from Griesswies, Rauris Valley, growing on euclase. **d** 3 mm sized and twinned cleft monazite (TAUERN1) on a quartz crystal. Erfurter Steig, Rauris Valley

1988). Analytical details and correction procedures closely follow those described in Kirkland et al. (2009) and Janots et al. (2012). Pb isotope signals were corrected for common Pb contribution using measured ^{204}Pb and a present day Pb isotope composition predicted by the model of Stacey and Kramers (1975). In monazite, ^{204}Pb is affected by an unresolvable molecular interference from doubly charged $^{232}Th^{144}Nd^{16}O_2^{++}$ (^{206}Pb and ^{207}Pb are also affected to a smaller degree by $ThNdO_2^{++}$), which can result in an over estimate of the amount of common Pb. The extent of this interference was monitored using $^{232}Th^{143}Nd^{16}O_2^{++}$ at mass 203.5 and a correction applied whenever the count rate exceeded the average background count on the ion-counting detector by three times its standard deviation. Age calculations were done using the decay constant recommendations of Steiger et al. (1977) and plots use the routines of Isoplot (Ludwig 2001) with uncertainties presented at the 2σ level. Th–Pb ages presented in the results section were calculated using common Pb and polyatomic Nd-overlap corrections.

Major and trace element concentrations of monazites were obtained by LA-ICP-MS system at the University of Bern using a GeoLas Pro 193 nm ArF Excimer laser system (Lambda Physik, Germany) coupled with an ELAN-DRCe quadrupole ICP-MS (Perkin Elmer, USA). Measurements closely followed procedures detailed in Pettke et al. (2012), employing an energy density of 4–5 Jcm^{-2} on the sample surface at 10 Hz laser repetition rate. Spot diameters varied between 24 and 60 µm. Analyses were made next to ion probe age dating spots. The ICP-MS settings were optimised to maximum signal to background intensity ratios with $(^{232}Th^{16}O)^{+}$ production rates below 0.5 % and robust plasma conditions as monitored by equal sensitivities of U and Th. Data reduction was done using SILLS (Guillong et al. 2008), with improved calculation of the limit of detection (Pettke et al. 2012), using the method without internal standard (Liu et al. 2008) and a sum of analysed oxides of 100 %. The synthetic SRM 610 glass from the National Institute of Standards and Technology (NIST) was used as the external standard.

4 Results

4.1 Age dating

All four dated cleft monazites are from the tectonically complex eastern region of the Tauern Window (Figs. 1, 2). Numbers in Fig. 4 refer to analysis spots.

Isotopic results for TAUERN1 show some compositional variations in the BSE image (Fig. 4a) that correlate with Th-U compositions (Tables 2, 3). A dark core (low in Th) is surrounded by brighter rim domains. Analysis point 21 is discarded due to its position on a crack expressed by an increased Th/U value of 27 (Table 3). Analyses in the darker core domain D1 in Fig. 4a gives a ^{232}Th-^{208}Pb age of 16.25 ± 0.55 Ma (MSWD = 3.0; spots 9–21; Fig. 5a). The three surrounding domains (D2–D4; Fig. 5a) give different ^{232}Th-^{208}Pb ages at 17.56 ± 0.55 Ma (MSWD = 1.6; spots 1–8), 15.00 ± 0.51 Ma (MSWD = 1.7; spots 22–29), and 18.99 ± 0.51 Ma (MSWD = 0.51; spots 30–34).

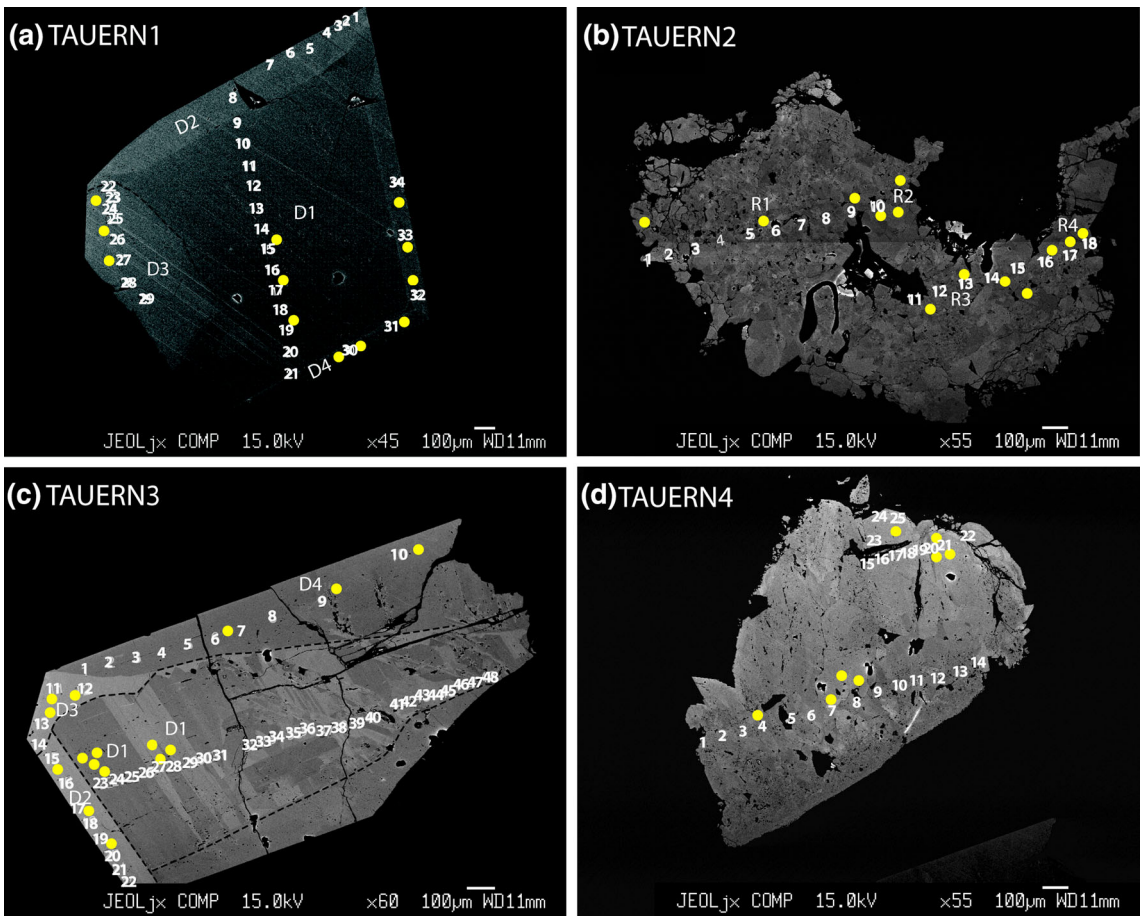

Fig. 4 BSE images of monazites showing *numbered ion* probe spot analyses. **a** TAUERN1; **b** TAUERN2; **c** TAUERN3 and **d** TAUERN4. The indicated spots are larger than the ion probe spot size. Numbers refer to Tables 3, 4, 5, 6. The *yellow spots* indicate LA-ICP-MS analysis spots. D and R refer to domains and regions addressed in the text

Table 2 Monazite LA–ICP–MS element concentrations (μg/g)

Element (isotope)	Tauern1a domain 2 (average ± σ)	Tauern1b domain 4 (average ± σ)	Tauern1c domain 1 (average ± σ)	Tauern1d domain 3 (average ± σ)	Tauern2a region 2 (average ± σ)	Tauern2b region 1 (average ± σ)	Tauern3a domain 3 (average ± σ)	Tauern3b domain 1 (average ± σ)	Tauern3c domain 1 (average ± σ)	Tauern3d domain 2 (average ± σ)	Tauern3e domain 2 (average ± σ)	Tauern4a region 1 (average ± σ)	Tauern4b region 2 (average ± σ)
Li7	bd	bd	bd	0.33 ± 0.11	bd	bd	8.1 ± 1.5	6.8 ± 1.2	7.0 ± 0.31	bd	2.8 ± 0.22	2 ± 2	0.57 ± 0.45
B11	bd	bd	bd	bd	bd	bd	1.1 ± 0.12	1.1 ± 0.064	0.71 ± 0.14	bd	0.51 ± 0.10	3.1 ± 2.2	bd
Na23	0.12 ± 0.01	bd	0.12 ± 0.02	0.130 ± 0.003	7 ± 6	1.0 ± 1.0	0.20 ± 0.06	0.46 ± 0.15	0.80 ± 0.28	0.16 ± 0.01	0.25 ± 0.04	56 ± 85	7.5 ± 2.5
Si29	bd	bd	bd	bd	bd	bd	760 ± 220	1400 ± 80	1400 ± 130	1850 ± 60	1770 ± 70	bd	bd
P31	123,300 ± 500	1,236,600 ± 400	123,200 ± 200	123,900 ± 400	123,000 ± 6000	116,000 ± 1800	115,800 ± 700	114,300 ± 300	113,100 ± 400	113,800 ± 400	113,600 ± 400	118,600 ± 700	118,000 ± 800
Ca43	520 ± 20	520 ± 20	1630 ± 90	1210 ± 60	2700 ± 800	2000 ± 600	7920 ± 30	11,500 ± 200	10,900 ± 140	7100 ± 400	8350 ± 120	1800 ± 900	970 ± 180
As75	328 ± 4	334 ± 5	335 ± 1	334 ± 1	335 ± 17	312 ± 4	3250 ± 60	3680 ± 30	3380 ± 70	2960 ± 90	2890 ± 50	780 ± 80	700 ± 50
Rb85	0.41 ± 0.02	0.41 ± 0.05	0.400 ± 0.005	0.49 ± 0.01	0.51 ± 0.13	0.47 ± 0.05	0.74 ± 0.02	1.10 ± 0.03	1.00 ± 0.07	1.10 ± 0.05	1.10 ± 0.04	0.50 ± 0.09	0.51 ± 0.10
Sr88	71.0 ± 0.9	70 ± 3	171 ± 6	158 ± 1	444 ± 37	380 ± 110	800 ± 20	1060 ± 20	1020 ± 10	570 ± 40	770 ± 4	160 ± 60	110 ± 20
Y89	5010 ± 50	5300 ± 100	5000 ± 100	6100 ± 200	6400 ± 1400	6300 ± 700	6620 ± 140	8330 ± 20	8100 ± 200	8500 ± 300	8090 ± 60	5200 ± 1300	5500 ± 700
Mo95	0.53 ± 0.05	0.59 ± 0.09	0.59 ± 0.03	0.61 ± 0.02	0.46 ± 0.03	0.52 ± 0.03	1.01 ± 0.04	1.29 ± 0.03	1.2 ± 0.20	0.90 ± 0.06	0.87 ± 0.10	0.90 ± 0.04	0.80 ± 0.07
La139	135,000 ± 1000	131,200 ± 1700	135,300 ± 600	132,800 ± 1100	133,000 ± 7000	136,000 ± 2000	131,000 ± 3000	136,800 ± 800	135,800 ± 1800	118,200 ± 400	127,300 ± 300	95,000 ± 4000	93,400 ± 1400
Ce140	281,900 ± 600	278,600 ± 1600	279,000 ± 1000	275,500 ± 700	290,000 ± 6000	293,940 ± 1500	272,300 ± 1400	269,800 ± 500	270,300 ± 1500	261,600 ± 1000	263,000 ± 11,000	242,000 ± 6500	239,100 ± 1100
Pr141	30,060 ± 10	30,250 ± 80	30,110 ± 100	29,590 ± 60	31,100 ± 1700	29,600 ± 300	30,350 ± 50	28,550 ± 50	28,900 ± 230	30,230 ± 40	29,270 ± 60	34,280 ± 330	33,970 ± 120
Nd146	114,500 ± 1000	117,000 ± 1000	116,600 ± 400	115,400 ± 1100	119,000 ± 3500	112,900 ± 2900	115,900 ± 1500	104,100 ± 300	106,500 ± 800	117,400 ± 400	110,800 ± 300	163,500 ± 1300	163,400 ± 1600
Sm147	20,600 ± 300	21,800 ± 400	21,300 ± 200	22,200 ± 300	23,700 ± 2300	20,500 ± 700	19,400 ± 500	17,130 ± 50	17,500 ± 200	20,650 ± 90	18,700 ± 140	39,000 ± 1600	40,900 ± 700
Eu151	3150 ± 30	3270 ± 70	3100 ± 30	3500 ± 20	3010 ± 230	2700 ± 400	2070 ± 30	1950 ± 10	1960 ± 20	2220 ± 10	2070 ± 20	5900 ± 400	6240 ± 80
Gd157	12,890 ± 180	13,800 ± 420	13,460 ± 110	15,070 ± 260	17,300 ± 1800	14,200 ± 500	11,700 ± 400	10,530 ± 60	10,620 ± 160	12,890 ± 160	11,510 ± 70	24,800 ± 2200	27,100 ± 600
Tb159	1140 ± 20	1230 ± 40	1170 ± 20	1360 ± 30	1600 ± 200	1290 ± 40	1040 ± 20	1034 ± 2	1030 ± 20	1210 ± 20	1100 ± 10	1980 ± 290	2150 ± 90
Dy161	3670 ± 40	3940 ± 120	3710 ± 60	4430 ± 70	4730 ± 350	4150 ± 120	3650 ± 100	4020 ± 20	3980 ± 70	4500 ± 110	4230 ± 30	5150 ± 780	5420 ± 380
Ho165	283 ± 4	304 ± 8	285 ± 6	350 ± 8	350 ± 60	335 ± 19	347 ± 7	423 ± 3	418 ± 9	452 ± 16	432 ± 2	350 ± 80	376 ± 43
Er167	276 ± 3	297 ± 8	279 ± 7	333 ± 11	330 ± 70	334 ± 34	524 ± 8	737 ± 3	716 ± 14	726 ± 32	706 ± 8	330 ± 90	351 ± 55
Tm169	11.0 ± 0.1	12.0 ± 0.2	11.0 ± 0.3	13.0 ± 0.5	14 ± 3	14 ± 2	39.0 ± 0.5	65.0 ± 0.1	62 ± 1	59 ± 3	59.0 ± 0.7	17 ± 5	17 ± 4
Yb173	22.0 ± 0.2	23.0 ± 0.2	24.0 ± 0.8	24.0 ± 1.2	30 ± 4	30 ± 4	141 ± 2	262 ± 1	250 ± 3	223 ± 11	226 ± 3	47 ± 15	49 ± 11
Lu175	0.96 ± 0.01	1.00 ± 0.02	1.00 ± 0.02	0.99 ± 0.05	1.50 ± 0.14	1.50 ± 0.22	8.8 ± 0.1	18.00 ± 0.05	17.0 ± 0.2	15.0 ± 0.8	15.0 ± 0.2	2.8 ± 0.9	2.8 ± 0.8
Wl82	0.120 ± 0.005	0.100 ± 0.009	0.12 ± 0.01	0.13 ± 0.01	0.13 ± 0.06	0.120 ± 0.006	0.26 ± 0.04	0.42 ± 0.04	0.36 ± 0.02	0.27 ± 0.02	0.27 ± 0.01	3 ± 3	0.54 ± 0.14
Bi209	0.007 ± 0.001	bd	0.004 ± 0.001	0.006 ± 0.001	bd	bd	31.0 ± 0.1	27.0 ± 0.3	26.0 ± 0.2	21 ± 1	22.0 ± 0.2	0.028 ± 0.008	0.025 ± 0.006
Th232	2980 ± 310	3800 ± 500	1510 ± 230	2750 ± 340	13,433 ± 17,718	700 ± 600	20,100 ± 900	29,870 ± 140	31,400 ± 2100	42,300 ± 300	41,530 ± 110	2300 ± 2000	4000 ± 1280
U238	480 ± 25	570 ± 70	260 ± 6	560 ± 14	570 ± 300	610 ± 70	20 ± 1	40.0 ± 0.2	40 ± 3	55 ± 2	49.0 ± 0.2	130 ± 35	163 ± 19

Be9, Mg25, Al27, Ti49, Mn55, Fe57, Te125 and Sb121 were analyzed but are also below detection. Numbers following the element refer to the isotope analyzed. Domain and region numbers according to age groups discussed in text

Bd below detection

Table 3 SIMS Th-U–Pb isotopic ratios, element concentrations and ^{232}Th-^{208}Pb ages of monazite TAUERN 1

Analysis ID	U (μg/g)	Th (μg/g)	Th/U measured	^{207}Pb/^{235}U	±σ (%)	^{206}Pb/^{238}U	±σ (%)	^{207}Pb/^{206}Pb	±σ (%)	^{208}Pb/^{232}Th	±σ (%)	Age (Ma) uncorr.	±σ (Ma)	Age (Ma) corrected	±σ (Ma)
Group 1															
n4198-Tauern1@01	195	2444	12.533	42.3	2.4	20.9	0.4	1533.8	99.9	15.7	1.5	18.20	0.50	17.82	0.50
n4198-Tauernl@02	348	2301	6.612	21.4	1.1	17.8	0.4	445.7	100.2	13.9	1.2	18.38	0.55	18.03	0.54
n4198-Tauernl@03	408	1984	4.863	23.6	1.3	19.6	0.4	452.1	109.7	17.3	1.6	17.90	0.57	17.61	0.56
n4198-Tauernl@04	334	2129	6.374	20.9	1.4	20.0	0.4	131.1	138.9	16.1	1.5	19.00	0.55	18.48	0.54
n4198-Tauernl@05	339	2709	7.991	23.9	1.4	20.1	0.4	426.7	119.0	18.6	1.7	18.13	0.49	17.84	0.50
n4198-Tauernl@06	431	2864	6.645	21.9	1.4	18.6	0.4	408.2	128.4	14.6	1.3	17.44	0.50	17.26	0.50
n4198-Tauernl@07	373	2713	7.273	19.5	1.0	17.8	0.4	244.5	108.7	13.8	1.2	17.39	0.56	17.18	0.55
n4198-Tauernl@08	493	2445	4.959	19.6	0.9	17.9	0.4	238.1	96.3	14.1	1.3	17.11	0.51	16.28	0.53
Group 2															
n4198-Tauernl@09	569	2443	4.293	18.8	0.9	17.8	0.4	151.7	95.8	14.6	1.3	17.76	0.54	17.14	0.55
n4198-Tauernl@10	194	1649	8.500	41.1	2.3	19.5	0.4	1606.9	94.8	15.2	1.4	17.02	0.54	15.10	0.53
n4198-Tauernl@11	202	1687	8.351	43.8	2.4	19.1	0.4	1765.3	90.2	15.0	1.4	16.69	0.51	14.55	0.51
n4198-Tauernl@12	198	1915	9.672	40.7	2.9	19.0	0.4	1638.0	123.5	14.8	1.5	17.53	0.57	16.45	0.55
n4198-Tauernl@13	198	2333	11.783	42.4	2.6	19.3	0.4	1681.8	103.7	15.2	1.5	17.85	0.53	17.00	0.55
n4198-Tauernl@14	209	2608	12.478	42.1	2.4	18.9	0.5	1703.4	94.5	15.1	1.4	17.14	0.53	16.44	0.51
n4198-Tauernl@15	222	2650	11.937	41.2	2.2	19.9	0.4	1567.8	91.6	15.1	1.4	17.36	0.50	16.17	0.51
n4198-Tauernl@16	216	2518	11.657	68.7	7.1	20.2	0.4	2476.7	166.1	15.0	1.4	17.59	0.60	15.81	0.55
n4198-Tauernl@17	201	2089	10.393	53.8	3.5	20.2	0.4	2040.6	108.1	15.2	1.4	17.80	0.54	16.52	0.57
n4198-Tauernl@18	208	2135	10.264	41.4	2.5	20.3	0.5	1543.8	101.5	15.0	1.4	16.93	0.59	15.15	0.56
n4198-Tauernl@19	214	2455	11.472	39.8	2.3	18.6	0.4	1636.3	98.1	14.6	1.4	18.14	0.54	17.39	0.56
n4198-Tauernl@20	195	3021	15.492	40.1	2.9	19.9	0.4	1522.4	127.2	14.3	1.3	16.97	0.49	16.04	0.47
Group 3															
n4198-Tauernl@22	456	3437	7.537	42.1	2.2	19.4	0.3	1663.0	91.9	17.6	1.7	16.42	0.42	15.04	0.41
n4198-Tauernl@23	541	2878	5.320	23.7	1.4	18.7	0.3	570.5	117.3	18.3	1.7	15.09	0.45	14.64	0.45
n4198-Tauernl@24	436	2432	5.578	25.3	1.7	18.4	0.4	742.8	134.3	17.0	1.6	17.02	0.50	16.25	0.49
n4198-Tauernl@25	506	2672	5.281	25.8	1.4	18.5	0.3	771.0	108.0	18.6	1.7	15.58	0.53	14.53	0.52
n4198-Tauernl@26	522	2839	5.439	23.0	1.3	17.7	0.3	622.8	109.1	15.9	1.5	15.60	0.44	15.52	0.47
n4198-Tauernl@27	394	4688	11.898	26.4	2.0	16.9	0.4	1006.5	141.0	12.8	1.3	15.43	0.48	14.70	0.47
n4198-Tauernl@28	221	3207	14.511	44.7	2.9	20.3	0.5	1684.2	109.0	15.8	1.5	16.04	0.45	15.04	0.45
n4198-Tauernl@29	232	2447	10.547	40.8	2.8	19.4	0.3	1596.3	120.8	16.1	1.6	15.42	0.47	14.25	0.51
Group4															
n4198-Tauernl@30	364	3597	9.882	19.8	1.4	18.9	0.4	131.6	148.5	15.5	1.4	18.09	0.71	18.03	0.72
n4198-Tauernl @31	416	3517	8.454	20.3	1.6	19.5	0.4	111.8	173.5	16.1	1.5	19.09	0.54	19.09	0.54
n4198-Tauernl@32	486	5097	10.488	19.6	1.1	19.0	0.4	102.9	122.7	15.4	1.4	19.63	0.54	19.09	0.53

Table 3 continued

Analysis ID	U (μg/g)	Th (μg/g)	Th/U measured	$^{207}Pb/^{235}U$	±σ (%)	$^{206}Pb/^{238}U$	±σ (%)	$^{207}Pb/^{206}Pb$	±σ (%)	$^{208}Pb/^{232}Th$	±σ (%)	Age (Ma) uncorr.	±σ (Ma)	Age (Ma) corrected	±σ (Ma)
n4198-Tauernl @33	362	3816	10.541	21.1	1.2	18.7	0.4	304.5	116.3	14.8	1.3	19.58	0.54	19.14	0.53
n4198-Tauernl @34	335	3743	11.173	23.9	1.4	19.2	0.5	527.4	112.5	15.0	1.4	19.90	0.53	19.16	0.53
Interface															
n4198-Tauernl @21	305	8385	27.492	24.3	1.3	18.9	0.3	593.4	107.0	13.8	1.2	17.58	0.44	17.40	0.45

Analysis ID refers to the analysis spots shown in Fig. 4

U–Pb ages are more complex. The $^{207}Pb/^{206}Pb$ intercept of domain1 is not compatible with a common Pb composition, thus the Tera-Wasserburg diagram is inappropriate. In fact, only domain 4 shows negligible common Pb and the lower intercept of the Tera-Wasserburg diagram yields age of 19.10 ± 0.57 Ma, in agreement with the ^{232}Th-^{208}Pb age.

Isotopic results for TAUERN2 are compiled in Table 4. Individual analysis spots (Fig. 4b) represent ages of one or mixed analyses of two of these grains. Monazites are characterised by low amounts of Th (9–8740 μg/g; Table 4) with Th/U values between 0.02 and 11. Analysis spot 04 lies on a fracture showing increased common Pb and has been excluded. Analysis spots 2, 5, 6, 8 (Fig. 5b) from region 1 have Th >1000 μg/g and give a ^{232}Th-^{208}Pb age of 15.12 ± 0.48 Ma (MSWD = 0.26). The other spots are too low in Th and have high initial Pb, thus robust ^{232}Th-^{208}Pb ages cannot be determined. However, in a Tera-Wasserburg diagram the U–Pb dataset yields a lower intercept age of 17.08 ± 0.27 Ma (MSWD = 1.19; Fig. 5b). Isotope analysis results are compiled in Table 4.

Isotopic results for TAUERN3 (Fig. 5c) show extreme Th/U ratios of up to ~1400. Four domains are distinguished texturally and by age determinations. The core of the crystal shows a complex growth zonation.

Core domain 1, characterised by similar U/Th values of the analysed spots, is the largest (Fig. 4c) and has the highest Th concentrations (Th > 40,000 μg/g). It has a $^{232}Th/^{208}Pb$ age of 15.49 ± 0.15 Ma (MSWD = 0.74; spots 23–48; Fig. 5c). Analysis points 23 and 32 have higher Th values and a higher apparent age. Domains 2 and 3 are darker in Fig. 4c but cannot be distinguished on the image. They have the lowest Th concentrations (Th < 20,000), but the highest Th/U ratios (>1090). Domain 2 gives a $^{232}Th/^{208}Pb$ age of 16.03 ± 0.27 Ma (MSWD = 0.51; spots 15–22; Fig. 5c). Domain 3 gives an age of 18.06 ± 0.42 Ma (MSWD = 0.51; spots 11–14; Fig. 5c), and domain 4 shows more scatter and yields an age of 17.18 ± 0.49 Ma (MSWD = 3.4; spots 1–10; Fig. 5c). Taking all 48 Th–Pb analyses together yields a geologically meaningless weighted mean age with a too high MSWD of 5.4. Due to the low U concentrations, U–Pb ages are imprecise, and the Tera-Wasserburg diagram gives an intercept age with a large error of 20.0 ± 5.2 Ma (MSWD = 0.93). Isotope analysis results are compiled in Table 5.

Isotopic results for TAUERN4 are compiled in Table 6. TAUERN4 (Fig. 4d) is an aggregate consisting of <10 μm-sized, zoned crystals with very variable Th concentrations ranging from 5 to 16,383 μg/g. Analysis spots with Th <200 μg/g gave unreliable ages. No correlation was detected between age and Th-U composition. For that reason all points are treated together resulting in an imprecise $^{232}Th/^{208}Pb$ age of 15.56 ± 0.70 Ma (MSWD = 9.1;

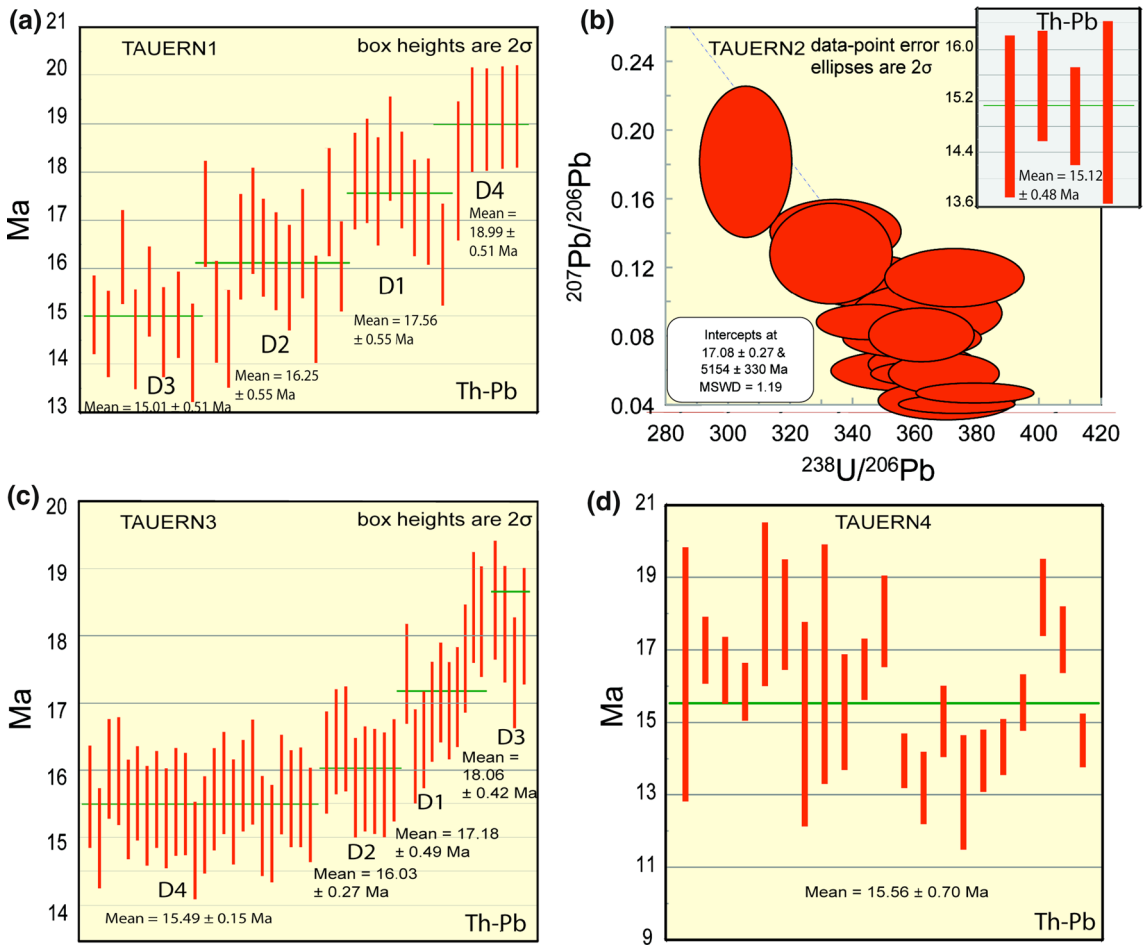

Fig. 5 ^{232}Th-^{208}Pb and Tera-Wasserburg ages of cleft monazites from samples TAUERN1–4

Fig. 5d). The high MSWD reflects the large scatter in the data. U values are <300 µg/g. The Tera-Wasserburg diagram shows variable amounts of common Pb with possible excess ^{206}Pb.

4.2 Monazite composition

LA-ICP-MS analyses are listed in Table 2 and analysis spots marked in yellow in Fig. 4. Analysis steps that showed Na spikes were interpreted as a mix with a fluid inclusion and discarded. All elements listed in Table 2 have been measured in comparable concentrations at three spots in the same growth zone. CI-chondrite-normalised (McDonough and Sun 1995) patterns of different domains in the four dated monazites show negative Eu anomalies (Fig. 6) and quite variable steepness, with La/Yb values ranging from 5600–6050 (TAUERN1) to 4430–4500 (TAUERN2), 521–930 (TAUERN3) and 1900–2000 (TAUERN4). Total REE concentrations show little variation (Table 2). By plotting La/Yb versus U, the four cleft monazites plot as individual clusters (Fig. 7a). The increased HREE concentrations in domains 1 and 2 (Table 2) of TAUERN3 correlate with an increased Y and Si content (thorite-huttonite, $ThSiO_4$, component). Average Th/U values vary from 4.4 to 7.2 (TAUERN1), 0.03–200 (TAUERN2), 740–1020 (TAUERN3) and 0.08–47 (TAUERN4). This compositional variation is displayed in Fig. 7b. A similar trend is observed when plotting As concentration (76–3233 µg/g; gasparite, $REEAsO_4$, component; Table 2) versus U (Fig. 7c). The monazites show 5400–7900 µg/g Y (xenotime, YPO_4, component) and ~1000–9200 µg/g Ca (brabantite, $CaTh(PO_4)_2$, component). Calcium correlates positively with 117–840 µg/g Sr (Table 2; Fig. 7d). Whereas As and Y are regularly distributed in the monazite, Ca and Sr show higher concentrations in the core regions of TAUERN 1 and 3 monazite. The analysed trace elements Be, Mg, Fe, and Te are below the detection limit. Sodium, Ti, and Bi are generally at or below the detection limit. Silicon and Bi are above the detection limit only in TAUERN3 (associated with tourmaline) and TAUERN4. Antimony is above the detection limit only in TAUERN4. Lithium is above the detection limit in some domains and regions of TAUERN1, 2 and 4

Table 4 SIMS Th-U–Pb isotopic ratios, element concentrations and ^{232}Th-^{208}Pb ages of monazite TAUERN 2

Analysis ID	U (µg/g)	Th (µg/g)	Th/U measured	^{207}Pb/^{235}U	±σ (%)	^{206}Pb/^{238}U	±σ (%)	^{207}Pb/^{206}Pb	±σ (%)	^{208}Pb/^{232}Th	±σ (%)	Age (Ma) uncorr.	±σ (Ma)	Age (Ma) corrected	±σ (Ma)
Spots >1000 ppm Th															
n4199-Tauern2@02	350	1578	4.509	0.04703	5.46	0.0029	2.26	0.00	10.37	0.000877	3.30	17.72	0.59	14.96	0.63
n4199-Tauern2@05	737	7666	10.402	0.02758	5.84	0.0028	1.81	0.00	9.69	0.000790	2.78	15.97	0.44	15.44	0.43
n4199-Tauern2@06	793	8744	11.026	0.02563	4.30	0.0027	1.75	0.00	9.74	0.000766	2.58	15.48	0.40	14.96	0.38
n4199-Tauern2@08	309	1061	3.434	0.05452	8.72	0.0030	2.18	0.00	9.71	0.000868	3.53	17.54	0.62	15.04	0.71
Spots <1000 ppm Th															
n4199-Tauern2@1	330	9	0.027	0.05926	5.45	0.0030	2.32	0.03	13.25	0.040115	4.04				
n4199-Tauern2@03	412	24	0.058	0.02662	6.94	0.0028	2.47	0.00	16.70	0.003491	8.39				
n4199-Tauern2@07	370	297	0.803	0.08111	9.36	0.0032	1.77	0.00	11.81	0.001655	8.70				
n4199-Tauern2@09	185	21	0.114	0.03797	7.24	0.0027	2.46	0.00	15.58	0.003821	10.31				
n4199-Tauern2@10	314	6	0.019	0.01971	8.41	0.0027	2.22	0.00	31.83	0.002578	21.56				
n4199-Tauern2@12	505	388	0.768	0.03315	5.50	0.0028	2.30	0.00	10.71	0.001277	5.46				
n4199-Tauern2@13	730	187	0.256	0.01882	4.43	0.0027	1.87	0.00	12.70	0.000933	5.88				
n4199-Tauern2@14	579	117	0.202	0.02523	6.99	0.0027	1.80	0.00	11.69	0.001867	5.29				
n4199-Tauern2@15	224	100	0.446	0.04437	5.90	0.0027	2.24	0.00	11.73	0.002169	5.44				
n4199-Tauern2@16	507	143	0.282	0.03801	4.45	0.0029	1.75	0.00	11.79	0.001704	6.62				
n4199-Tauern2@17	363	173	0.477	0.03367	6.95	0.0028	1.75	0.00	12.66	0.001228	7.33				
n4199-Tauern2@18	847	410	0.484	0.02073	4.24	0.0026	1.87	0.00	10.14	0.000908	4.70				
Interface															
n4199-Tauern2@04	567	401	0.707	1.22381	3.31	0.0131	2.87	0.03	10.59	0.030195	4.64				

Analysis ID refers to the analysis spots shown in Fig. 4

Table 5 SIMS Th-U–Pb isotopic ratios, element concentrations and ^{232}Th-^{208}Pb ages of monazite TAUERN 3

Analysis ID	U (μg/g)	Th (μg/g)	U/Th measured	^{207}Pb/^{235}U	±σ (%)	^{206}Pb/^{238}U	±σ (%)	^{207}Pb/^{206}Pb	±σ (%)	^{208}Pb/^{232}Th	±σ (%)	Age (Ma) uncorr.	±σ (Ma)	Age (Ma) corrected	±σ (Ma)
Group 1															
n4200-Tauern3@1	15	18,447	1255.305	14.12581	2.83	0.1262	2.14	14.12581	2.83	0.001101	2.51	22.24	0.56	17.44	0.37
n4200-Tauern3@02	16	17,771	1091.340	14.29928	3.41	0.1236	1.75	14.29928	3.41	0.001032	2.49	20.84	0.52	16.22	0.35
n4200-Tauern3@03	16	18,502	1129.833	No data	No data	0.1381	2.08	No data	No data	0.001032	2.49	20.84	0.52	16.46	0.36
n4200-Tauern3@04	15	17,856	1180.209	17.33225	2.90	0.1517	1.91	17.33225	2.90	0.001056	2.50	21.33	0.53	16.88	0.37
n4200-Tauern3@05	15	18,936	1225.547	No data	No data	0.1399	2.35	No data	No data	0.001079	2.49	21.79	0.54	17.16	0.37
n4200-Tauern3@06	16	19,417	1187.925	No data	No data	0.1446	1.82	No data	No data	0.001065	2.51	21.51	0.54	16.90	0.36
n4200-Tauern3@07	16	19,172	1226.956	No data	No data	0.1575	1.92	No data	No data	0.001088	2.51	21.98	0.55	17.10	0.37
n4200-Tauern3@08	14	18,119	1255.827	No data	No data	0.1511	1.91	No data	No data	0.001124	2.55	22.70	0.58	17.67	0.40
n4200-Tauern3@09	15	18,752	1237.845	No data	No data	0.1646	2.67	No data	No data	0.001221	2.49	24.66	0.61	18.43	0.41
n4200-Tauern3@10	14	19,058	1323.294	15.29356	2.54	0.1369	1.91	15.29356	2.54	0.001142	2.58	23.07	0.59	18.22	0.41
Group 2															
n4200-Tauern3@11	40	38164	945.548	2.98173	2.96	0.0283	1.76	2.98173	2.96	0.000979	2.49	19.78	0.49	18.53	0.44
n4200-Tauern3@12	42	34,335	813.622	No data	No data	0.0376	1.80	No data	No data	0.000977	2.49	19.74	0.49	18.18	0.43
n4200-Tauern3@13	43	41,062	950.226	2.92995	3.59	0.0278	1.77	2.92995	3.59	0.000920	2.49	18.59	0.46	17.45	0.41
n4200-Tauern3@14	39	43,541	1114.689	No data	No data	0.0357	2.05	No data	No data	0.000964	2.50	19.47	0.49	18.15	0.43
n4200-Tauern3@15	59	45,738	778.976	4.11090	3.51	0.0381	2.11	4.11090	3.51	0.000852	2.50	17.22	0.43	16.12	0.38
n4200-Tauern3@16	49	46,269	937.275	4.33713	3.47	0.0410	2.50	4.33713	3.47	0.000880	2.55	17.78	0.45	16.43	0.39
n4200-Tauern3@17	47	42,531	902.921	No data	No data	0.0374	1.83	No data	No data	0.000872	2.53	17.62	0.45	16.47	0.39
n4200-Tauern3@18	54	41,739	777.038	4.12162	3.26	0.0387	1.75	4.12162	3.26	0.000840	2.52	16.98	0.43	15.75	0.37
n4200-Tauern3@19	56	46,107	821.224	No data	No data	0.0344	1.90	No data	No data	0.000835	2.54	16.86	0.43	15.89	0.39
n4200-Tauern3@20	54	45,228	834.498	No data	No data	0.0406	1.75	No data	No data	0.000847	2.60	17.11	0.45	15.85	0.39
n4200-Tauern3@21	60	42,519	707.836	No data	No data	0.0457	1.91	No data	No data	0.000845	2.60	17.06	0.44	15.80	0.39
n4200-Tauern3@22	49	45,971	935.744	No data	No data	0.0421	1.80	No data	No data	0.000845	2.50	17.07	0.43	16.01	0.38
n4200-Tauern3@23	24	29,085	1207.287	No data	No data	0.0987	2.09	No data	No data	0.001033	2.49	20.88	0.52	17.44	0.38
n4200-Tauern3@24	56	33,544	604.381	No data	No data	0.0805	1.85	No data	No data	0.000883	2.63	17.84	0.47	15.61	0.38
n4200-Tauern3@25	39	28,035	716.047	15.36243	3.17	0.1396	1.98	15.36243	3.17	0.000926	2.83	18.71	0.53	14.99	0.37
n4200-Tauern3@26	59	36,404	616.284	8.20173	2.93	0.0740	1.80	8.20173	2.93	0.000910	2.54	18.38	0.47	16.02	0.37
n4200-Tauern3@27	69	37,353	544.260	9.15241	3.67	0.0800	2.54	9.15241	3.67	0.000911	2.54	18.40	0.47	15.99	0.40
n4200-Tauern3@28	60	29,096	487.879	12.16617	2.91	0.1088	1.75	12.16617	2.91	0.000938	2.74	18.95	0.52	15.42	0.37
n4200-Tauern3@29	51	36,403	710.645	No data	No data	0.0631	1.80	No data	No data	0.000903	2.53	18.24	0.46	15.66	0.35
n4200-Tauern3@30	63	32,070	511.927	8.42848	3.00	0.0769	1.74	8.42848	3.00	0.000906	2.66	18.30	0.49	15.33	0.37
n4200-Tauern3@31	61	30,220	498.030	8.51136	2.94	0.0789	1.75	8.51136	2.94	0.000922	2.51	18.64	0.47	15.57	0.36
n4200-Tauern3@32	13	14,999	1134.090	No data	No data	0.1956	2.00	No data	No data	0.001130	2.57	22.83	0.59	17.22	0.39
n4200-Tauern3@33	23	17,163	750.823	17.46494	3.45	0.1511	1.87	17.46494	3.45	0.000946	2.52	19.12	0.48	15.29	0.37
n4200-Tauern3@34	53	28,490	535.430	No data	No data	0.0550	1.79	No data	No data	0.000869	2.76	17.55	0.48	15.53	0.40

Table 5 continued

Analysis ID	U (μg/g)	Th (μg/g)	U/Th measured	$^{207}Pb/^{235}U$	±σ (%)	$^{206}Pb/^{238}U$	±σ (%)	$^{207}Pb/^{206}Pb$	±σ (%)	$^{208}Pb/^{232}Th$	±σ (%)	Age (Ma) uncorr.	±σ (Ma)	Age (Ma) corrected	±σ (Ma)
n4200-Tauern3 @3 5	32	18659	580.511	No data	No data	0.0357	3.19	No data	No data	0.000846	2.57	17.09	0.44	15.50	0.38
n4200-Tauern3@36	38	19,878	520.835	No data	No data	0.0322	1.78	No data	No data	0.000806	2.49	16.29	0.40	14.81	0.36
n4200-Tauern3@37	28	21,698	776.787	No data	No data	0.0501	1.84	No data	No data	0.000871	2.54	17.59	0.45	15.19	0.36
n4200-Tauern3 @3 8	42	22,843	548.354	No data	No data	0.0627	1.76	No data	No data	0.000870	2.59	17.58	0.46	15.57	0.38
n4200-Tauern3@39	27	20,925	786.290	9.07943	2.96	0.0858	1.76	9.07943	2.96	0.000944	2.49	19.07	0.47	15.81	0.38
n4200-Tauern3@40	27	16,305	606.847	No data	No data	0.0715	1.77	No data	No data	0.000898	2.73	18.15	0.49	15.39	0.39
n4200-Tauern3@41	24	19,087	806.700	8.04251	2.83	0.0759	1.76	8.04251	2.83	0.001007	2.49	20.35	0.51	15.77	0.34
n4200-Tauern3@42	56	33,218	591.753	No data	No data	0.0667	2.11	No data	No data	0.000905	2.66	18.29	0.49	15.98	0.39
n4200-Tauern3@43	58	27,239	466.568	No data	No data	0.0501	1.80	No data	No data	0.000851	2.51	17.19	0.43	15.17	0.37
n4200-Tauern3@44	48	22,097	462.178	6.87396	3.71	0.0631	2.08	6.87396	3.71	0.000871	2.51	17.59	0.44	15.06	0.36
n4200-Tauern3@45	68	30,313	443.708	5.53553	3.32	0.0517	1.74	5.53553	3.32	0.000886	2.49	17.89	0.44	15.79	0.37
n4200-Tauern3@46	63	35,556	562.233	5.53183	2.90	0.0497	1.75	5.53183	2.90	0.000889	2.58	17.96	0.46	15.58	0.36
n4200-Tauern3@47	43	25,506	598.604	8.51217	3.19	0.0759	1.83	8.51217	3.19	0.000918	2.58	18.54	0.48	15.60	0.37
n4200-Tauern3@48	26	19,177	732.107	11.34335	3.66	0.1006	1.78	11.34335	3.66	0.000944	2.49	19.08	0.48	15.34	0.35

Analysis ID refers to the analysis spots shown in Fig. 4

(Table 2). The fourstudied monazites also systematically show 0.42–1.01 μg/g Rb, 0.5 μg/g Mo and ~0.1-2.5 μg/g W.

5 Discussion

5.1 Age dating

Whereas the core and rims of TAUERN1 give well-resolved ^{232}Th-^{208}Pb ages of 15.00 ± 0.51 to 18.99 ± 0.51 Ma, the age distribution within the crystal is puzzling because there is no obvious relationship between the geometry of the growth zones and the age as observed in other cases (Janots et al. 2012; Berger et al. 2013). This suggests that growth was either more complicated than suggested by BSE imaging (Fig. 4a), or more likely, not all growth zones are cut by the section analyzed. We can also not exclude that the patchy core region of TAUERN3 represent a zone of monazite replacement. However, this needs to be confirmed by other monazite examples.

TAUERN2 yielded a ^{232}Th-^{208}Pb mean crystallization age of 15.12 ± 0.48 Ma, based only on four spots containing sufficient Th. The well-defined U–Pb age of 17.08 ± 0.27 Ma, based on all the analysis spots from TAUERN2, is comparable to the monazites, despite occurring as a crust consisting of tiny monazites (Fig. 4b). This suggests that Be-mineral bearing clefts do not represent a separate, younger generation of clefts. Rather the occurrence of Be minerals seems to be controlled by the host rock containing Be-bearing biotite (e.g., Weiss et al. 2005).

TAUERN3 is comparable to TAUERN1 and yields ^{232}Th-^{208}Pb domain ages between 15.49 ± 0.15 and 18.06 ± 0.42 Ma. TAUERN4, which also consists of an aggregate of small monazite grains, gives an imprecise average ^{232}Th-^{208}Pb age of 15.56 ± 0.70 Ma. This age also falls in the age range obtained with the other samples.

The obtained age results indicate that all four cleft monazites crystallised between ~19 and 15 Ma and that there is no resolvable age difference between large monazites and monazite crusts. The data also confirm that hydrothermal monazite can only be dated reliably with the ^{232}Th-^{208}Pb system (see discussion in Janots et al. 2012), but that in rare cases, here strongly reduced host rocks, the U–Pb dating of low Th/U hydrothermal monazites may also yield reliable ages.

5.2 Mineral composition

Chemical and isotopic results indicate that each monazite occurrence has distinct U, Th, La/Yb, As and Ca (Sr) concentrations. Uranium and La/Yb are the most

Table 6 SIMS Th-U–Pb isotopic ratios, element concentrations and ^{232}Th-^{208}Pb ages of monazite TAUERN 4

Analysis ID	U (μg/g)	Th (μg/g)	Th/U measured	^{207}Pb/^{235}U	±σ (%)	^{206}Pb/^{238}U	±σ (%)	^{207}Pb/^{206}Pb	±σ (%)	^{208}Pb/^{232}Th	±σ (%)	Age (Ma) uncorr.	±σ (Ma)	Age (Ma) corrected	±σ (Ma)
Analyses >200 ppm Th															
n4201 -Tauern4@03	74	918	12.405	0.80966	8.57	0.0093	7.53	0.00214	14.41	0.001762	10.61	35.59	3.77	16.32	1.75
n4201 -Tauern4@06	113	3885	34.381	0.26638	6.38	0.0053	3.99	0.00178	12.61	0.000913	2.63	18.44	0.48	16.99	0.46
n4201 -Tauern4@07	175	6645	37.971	0.10817	7.43	0.0033	2.49	0.00107	10.91	0.000846	2.59	17.08	0.44	16.45	0.46
n4201 -Tauern4@08	200	8671	43.355	0.04794	6.54	0.0030	2.17	0.00097	9.37	0.000813	2.51	16.43	0.41	15.86	0.40
n4201 -Tauern4@09	254	361	1.421	0.05539	10.39	0.0032	1.79	0.00161	12.35	0.001207	4.79	24.38	1.17	18.27	1.13
n4201-Tauern4@10	112	1000	8.929	0.39082	4.09	0.0061	1.94	0.00188	9.74	0.001509	2.58	30.47	0.78	17.98	0.76
n4201-Tauern4@l 1	64	234	3.656	0.44071	5.55	0.0073	1.97	0.00283	17.26	0.002730	6.08	55.11	3.35	14.94	1.41
n4201-Tauern4@12	174	221	1.270	0.11172	4.90	0.0035	2.04	0.00228	10.19	0.002318	5.14	46.80	2.40	16.63	1.65
n4201-Tauern4@13	161	1114	6.919	0.07708	7.47	0.0031	3.11	0.00095	10.28	0.000915	3.39	18.49	0.63	15.30	0.80
n4201-Tauern4@14	68	15,849	233.074	0.10970	8.63	0.0045	2.47	0.00078	9.61	0.000834	2.54	16.85	0.43	16.48	0.42
n4201-Tauern4@15	115	1695	14.739	0.05014	7.92	0.0032	3.80	0.00090	10.24	0.000917	3.09	18.53	0.57	17.80	0.63
n4201-Tauern4@16	181	2474	13.669	0.04007	12.37	0.0033	3.44	0.00144	11.27	0.000690	2.75	13.95	0.38	13.95	0.38
n4201-Tauern4@17	267	1967	7.367	0.05389	9.72	0.0032	3.50	0.00158	11.39	0.000743	2.75	15.02	0.41	13.21	0.50
n4201-Tauern4@18	237	2791	11.776	0.05226	10.84	0.0033	2.55	0.00167	10.99	0.000774	3.05	15.65	0.48	15.04	0.49
n4201-Tauern4@19	118	799	6.771	0.06401	14.76	0.0034	6.01	0.00157	13.90	0.000711	4.94	14.37	0.71	13.09	0.79
n4201 -Tauern4@20	182	2759	15.159	0.03484	15.65	0.0034	3.92	0.00150	11.50	0.000719	2.76	14.53	0.40	13.95	0.43
n4201-Tauern4@21	213	5493	25.789	0.02469	14.11	0.0030	3.21	0.00158	10.92	0.000718	2.72	14.50	0.39	14.34	0.39
n4201 -Tauern4@22	42	16384	390.095	0.16248	7.95	0.0060	2.31	0.00082	10.19	0.000784	2.51	15.83	0.40	15.58	0.39
n4201 -Tauern4@23	121	3873	32.008	0.03395	7.69	0.0031	2.63	0.00082	9.49	0.000933	2.78	18.85	0.52	18.46	0.53
n4201 -Tauern4@24	63	9759	154.905	0.06,485	11.56	0.0037	3.14	0.00079	10.15	0.000860	2.58	17.37	0.45	17.28	0.46
n4201 -Tauern4@25	106	9616	90.717	0.03834	13.38	0.0039	4.58	0.00133	11.24	0.000728	2.50	14.72	0.37	14.51	0.37
Analyses <200 ppm Th															
n4201-Tauern4@l	133	108	0.812	0.60490	3.90	0.0074	1.75	0.01287	9.71	0.009822	2.55				
n4201 -Tauern4@02	87	50	0.575	No data	No data	0.0170	1.75	0.05006	9.73	0.037260	2.50				
n4201 -Tauern4@04	61	5	0.082	0.55549	5.96	0.0076	1.86	0.11078	11.37	0.115780	2.88				
n4201 -Tauern4@05	66	189	2.864	0.36172	7.11	0.0062	2.59	0.00327	10.73	0.003468	3.86				

Analysis ID refers to the analysis spots shown in Fig. 4

discriminative (Figs. 6, 7a). As all four clefts occur in rocks with identical peak metamorphic conditions (Scharf et al. 2013), the observed compositional variations between the cleft monazites seems to be controlled by the oxidation state of the fluid, which presumably is regulated by the oxidation state of the host rock. Whereas monazites TAUERN1 and 2 are from clefts in graphite-bearing schists ("Schwarzschiefer"), TAUERN3 is hosted in a strongly oxidised Permo-Triassic meta-arenite where monazite occurs in association with hematite. The gneiss hosting TAUERN4 has an intermediate oxidation state. The relationship between the cleft monazite composition and the oxidizing/reducing host rock lithology is underlined by the arrows in Fig. 7a–c. Under oxidizing conditions As is pentavalent and enters the monazite structure, replacing P (e.g., Janots et al. 2006, 2011; Ondrejka et al. 2007; Fig. 7c). Under more reducing conditions As is probably trivalent or monovalent and goes in cleft sulphides, mainly pyrite (Liang et al. 2013). The negative Eu anomaly in the chondrite-normalised monazite REE patterns (Fig. 6) is interpreted as being inherited from the sedimentary protolith or metamorphic paragenesis. Metamorphic minerals like garnet (HREE host) or hornblende (MREE host), that could influence the REE patterns of the cleft monazite, do not occur in the host rocks. For this reason dissolution of accessory minerals, e.g., monazite, xenotime, fluorapatite, allanite, feldspar and carbonates, likely provided the REEs for the cleft monazite. The fact that some clefts in the Lohninger quarry contain tens of grams of loose monazite (Josef Rathgeb pers. com., 2013) suggests that strings of REE-mineral enriched placers occur in the meta-arenite exploited in the quarry. The correlation of Ca and Sr (Fig. 7d) indicates dissolution of host-rock plagioclase or carbonates as a source. Increased Sr values in TAUERN2 indicate an additional source. Evidence of fluorapatite dissolution (high in LREE or MREE) is only recognizable in TAUERN4.

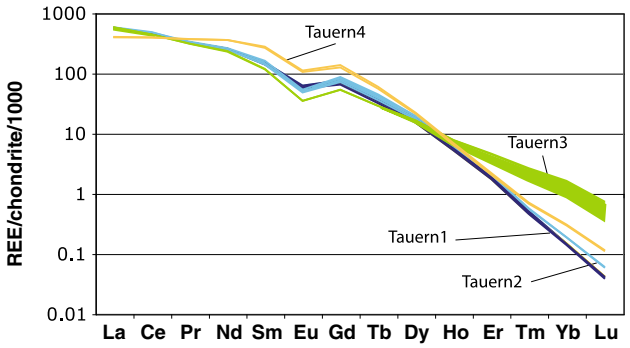

Fig. 6 Chondrite-normalised LA–ICP–MS REE patterns of the four monazites from the Tauern Window. Variation in slope of the monazite REE patterns

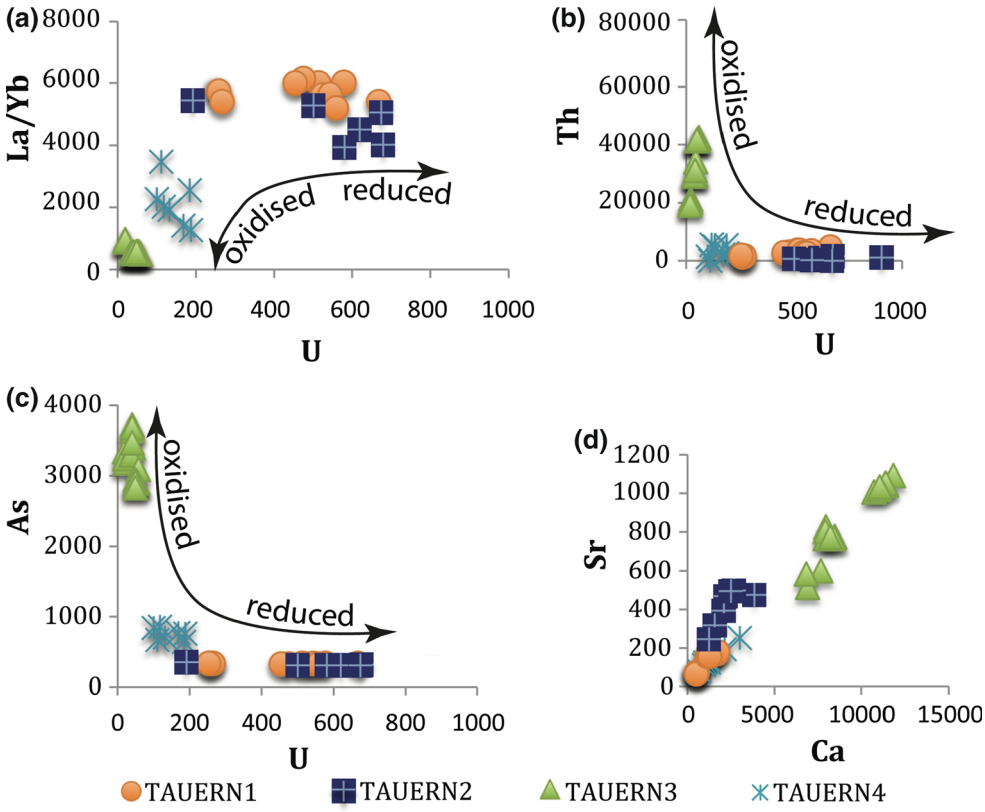

Fig. 7 Compositional variation in TAUERN1–4. The *arrows* in plots **a**–**c** indicate trends related to more oxidizing/reducing conditions

Monazite TAUERN3, which crystallised with tourmaline, shows very low concentrations of B that correlate with Li concentrations in four of the five analysed domains (Table 2). Monazite TAUERN2 that crystallised with the Be-mineral euclase in Be-bearing biotite schists (Weiss et al. 2005) hosts less than 0.4 µg/g Be (Table 2). The analysed Na in some monazite domains probably reflects the presence of tiny NaCl-bearing fluid inclusions.

The larger cleft monazites have chemically variable domains expressed by variable Th/U values (Fig. 4; Tables 2, 3, 4, 5, 6) in agreement with the data of Janots et al. (2012) and Berger et al. (2013). Monazite TAUERN3 shows extreme Th/U ratios of up to ~1400. The results show that TAUERN3 and TAUERN4 Th/U values plot in the field of hydrothermal monazite proposed by Janots et al. (2012). In contrast, TAUERN1 and 2 from the "Schwarzschiefer" (graphite-bearing host rock) show Th/U values characteristic of monazite in medium-grade metamorphic rocks. This suggests that more oxidizing conditions (TAUERN3 and 4) are required so that hexavelent U is not incorporated in monazite but remains in the fluid (Janots et al. 2012). Indeed, the U^{6+}-bearing mineral cleusonite, $(Pb,Sr)(U^{4+},U^{6+})(Fe^{2+},Zn)_2(Ti,Fe^{2+},Fe^{3+})_{18}(O,OH)_{38}$, is reported in hematite-monazite-bearing clefts of the Lohninger Quarry.

Xenotime has been reported in cleft TAUERN2 (Niedermayr et al. 2010). If xenotime had crystallized coevally with monazite, it would be possible to use the monazite-xenotime thermometer (e.g., Heinrich et al. 1997). However, the mol. fraction of $HREE_{Gd\text{-}Yb}$ in TAUERN2 is 0.06–0.07, indicating unrealistic temperatures of ~500–550 °C. It hence seems that xenotime crystallization was not in equilibrium with monazite.

The four studied cleft monazites thus document very nicely that cleft monazite composition is controlled by host-rock composition, which controls the composition of the mineralising fluid. The prevailing oxygen fugacity seems to have a major influence on monazite composition too.

5.3 Exhumation

The obtained ~19–15 Ma cleft monazite crystallization ages in the eastern part of the Tauern Window can be compared with published zircon fission track and zircon (U–Th)/He cooling data from the same area (Dunkl et al. 2003; Wölfler 2008). Our results show that cleft monazite crystallization ages are coeval to slightly younger than zircon fission track ages (Fig. 8) with an estimated closure temperature between 240 and 280 °C (Yamada et al. 1995; Bernet and Garver 2005; Reiners 2005; Bernet 2009). However, the monazite crystallization ages are older than the (U–Th)/He zircon ages (Wölfler et al. 2012) with a closure temperature in the range of 150–220 °C (Bernet and Garver 2005; Reiners 2005). Comparable observations have been made in the southern Aar Massif (Berger et al. 2013). This suggests that, in contrast to monazite in rocks, stepwise monazite crystallization in clefts may occur at or below the zircon fission track closure temperature of 280–240 °C during exhumation, and in combination with complex fluid/rock interaction in variably oxidised host rocks.

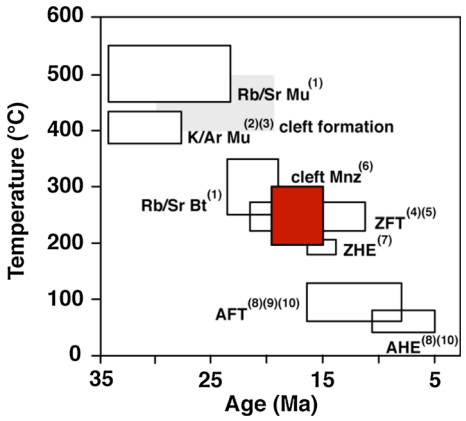

Fig. 8 Compilation of thermochronological data for the Sonnblick area given in Wölfler et al. (2012). The zircon fission track and (U–Th)/He data constrain the crystallization temperature of the cleft monazite ages from the Sonnblick region to ~300–200 °C. *Mu* muscovite, *Bt* biotite, *Mnz* monazite crystallization, *ZFT* zircon fission track, *ZHe* zircon (U–Th)/He, *AFT* apatite fission track, *AHe* apatite (U–Th/He). *1* Reddy et al. (1993); *2* Lambert (1970); *3* Waters (1976); *4* Dunkl et al. (2003); *5* Bertrand (2013); *6* this study; *7* Wölfler et al. (2012); *8* Wölfler (2008); *9* Staufenberg (1987); *10* Foeken et al. (2007). The *grey box* indicates temperature estimates for cleft formationin metamorphic domes, based on fluid inclusion studies (e.g., Luckscheiter and Morteani 1980; Mullis et al. 1994)

6 Conclusions

The cleft formation in the Sonnblick region of the Tauern Window occurred during metamorphic doming in association with E-W extension, as indicated by the cleft orientation perpendicular to foliation and stretching lineation (Fig. 2). This occurred at the stress field of the main ductile deformation. Cleft formation is most likely controlled by local competence contrast and/or fluid enhanced embrittlement during overall ductile deformation. The time and PT conditions of the cleft formation are not well known. However, in comparison with other Alpine metamorphic dome regions, formation occurred probably at 450 ± 50 °C (Luckscheiter and Morteani 1980; Mullis et al. 1994; Fig. 8). Monazite crystallization in the clefts occurred a few million years later, ~19–15 Ma ago, at the end of crystallization of quartz and adularia in the clefts,

and at temperatures of ~300–200 °C. The Tauern Au veins are only at small angle to the alpine cleft orientation (Fig. 2). This suggests that they probably formed in the same stress field slightly before or after the cleft formation.

Acknowledgments The Nordsims ion microprobe facility is operated by the research funding agencies of Denmark, Iceland, Norway, and Sweden, the Geological Survey of Finland and the Swedish Museum of Natural History. André Piuz is thanked for helping with the SEM and Peter Schmitzer for guiding us in the field. We thank Claudio Rosenberg and an anonymous reviewer, as well as Daniel E. Harlov, Antonio Langone,and Marco Scambelluri for thorough reviews of the manuscript. The project was partially funded by the Swiss National Foundation grant 200021-143972.

References

Berger, A., Gnos, E., Janots, E., Whitehouse, M., Soom, M., Frei, R., & Waight, T. E. (2013). Dating brittle tectonic movements with cleft monazite: fluid-rock interaction and formation of REE minerals. *Tectonics, 32*, 1–14.

Berger, A., Gnos, E., Schreurs, G., Fernandez, A., & Rakotondrazafy, M. (2006). Late Neoproterozoic, Ordovician and Carboniferous events recorded in monazites from south-central Madagascar. *Precambrian Research, 144*, 287–296.

Bernet, M. (2009). A field-based estimate of the zircon fission-track closure temperature. *Chemical Geology, 259*, 181–189.

Bernet, M., Garver, J. I. (2005). Fission track analysis of detrital zircon. In: P. W. Reiners, T. A. Ehlers (Eds.), *Low-temperature thermochronology* (pp.205–179). Chantilly, Virginia, Mineralogical Society of America, 58.

Bertrand, A. (2013). Exhuming the core of collisional orogens, the Tauern Window (Eastern-Alps). A geochronological, modelling and structural study. PhD-thesis, Freie Universität Berlin, Berlin, pp 175.

Cherniak, D. J., Watson, E. B., Grove, M., & Harrison, T. M. (2004). Pb diffusion in monazite: a combined RBS/SIMS study. *Geochimica et Cosmochimica Acta, 68*, 829–840.

Christensen, J. N., Selverstone, J., Rosenfeld, J. L., & DePaolo, D. J. (1994). Correlation by Rb-Sr geochronology of garnet growth histories from different structural levels within the Tauern Window, Eastern Alps. *Contributions to Mineralogy and Petrology, 118*, 1–12.

Corfu, F. (1988). Differential response of U-Pb systems in coexisting accessory minerals, Winnipeg River Subprovince, Canadian Shield: implications for Archean crustal growth and stabilization. *Contribution to Mineralogy and Petrology, 98*, 312–325.

Didier, A., Bosse, V., Boulvais, P., Bouloton, J., Paquette, J.-L., Montel, J.-M., & Devidal, J.-L. (2013). Disturbance versus preservation of U-Th-Pb ages in monazites during fluid-rock interaction: textural, chemical and isotopic in situ study in microgranites (Veley Dome, France). *Contributions to Mineralogy and Petrology, 165*, 1051–1072.

Dunkl, I., Frisch, W., & Grundmann, G. (2003). Zircon fission track thermochronology of the southeastern part of the Tauern Window and the adjacent Austoalpine margin, Eastern Alps. *Eclogae Geologicae Helveticae, 96*, 209–217.

Exner, C. (1962). *Geologische Karte der Sonnblickgruppe 1:50000*. Wien: Geologische Bundesanstalt.

Feitzinger, G., & Paar, W. H. (1991). Gangförmige Gold-Silber-Vererzungen in der Sonnblickgruppe (Hohe Tauern, Kärnten). *Archiv für Lagerstättenforschung der Geologischen Bundesanstalt, 13*, 17–50.

Foeken, J. P. T., Persano, C., Stuart, F. M., Voorde, T. M. (2007). Role of topography in isotherm perturbation: apatite (U–Th)/He and fission track results from the Malta Tunnel, Tauern Window, Austria. *Tectonophysics, 26*, TC 3006. doi:10.1029/2006TC002049.

Frasl, G. (1958). Zur Seriengliederung der Schieferhülle in den mittleren Hohen Tauern. *Jahrbuch für Geologie, 101*, 323–472.

Frisch, W., Dunkl, I., & Kuhlemann, J. (2000). Post-collisional orogen-parallel large-scale extension in the Eastern Alps. *Tectonophysics, 327*, 239–265.

Gasquet, D., Bertrand, J.-M., Paquette, J.-L., Lehmann, J., Ratzov, G., De Ascencao Guedes, R., et al. (2010). Miocene to Messinian deformation and hydrothermal activity in a pre-Alpine basement massif of the French western Alps: new U-Th-Pb and Argon ages from the Lauzière massif. *Bulletin de la Société Géologique de France, 181*, 227–241.

Guillong, M., Meier, D.L., Allan, M. M., Heinrich, C. A. (2008). SILLS: a MATLAB-based program for the reduction of laser ablation ICP-MS data of homogeneous materials and inclusions. In: P. J. Sylvester (Ed), *Laser ablation ICP-MS in the Earth Sciences: Current practices and outstanding issues* (pp. 328–333). Toronto, Mineralogical Association of Canada Short Course Series.

Harlov, D. E., Wirth, R., & Hetherington, C. J. (2011). Fluid-mediated partial alteration in monazite: the role of coupled dissolution-precipitation in element distribution and mass transfer. *Contributions to Mineralogy and Petrology, 162*, 329–348.

Harrison, T. M., McKeegan, K. D., & LeFort, P. (1995). Detection of inherited monazite in the Manaslu leucogranite by $^{208}Pb/^{232}Th$ ion microprobe dating: crystallization age and tectonic implications. *Earth and Planetary Science Letters, 133*, 271–282.

Heinrich, W., Andrehs, G., & Franz, G. (1997). Monazite-xenotime miscibility gap thermometry, 1. An empirical calibration. *Journal of Metamorphic Geology, 15*, 3–16.

Hejl, E. (1998). Über die känozoische Abkühlung und Denudation der Zentralalpen östlich der Hohen Tauern—eine Apatit-Spaltspuranalyse. *Mitteilungen der Österreichischen Geologischen Gesellschaft, 89*, 179–199.

Hetherington, C. J., Harlov, D. E., & Budzyn, B. (2010). Experimental metasomatism of monazite and xenotime: mineral stability, REE mobility and fluid composition. *Mineralogy and Petrology, 99*, 165–184.

Hoinkes, G., Koller, F., Ranitsch, G., Dachs, E., Hock, V., Neubauer, F., & Schuster, R. (1999). Alpine metamorphism of the Eastern Alps: thermochronological interpretation of apatite fission-track data. *Tectonophysics, 272*, 159–174.

Hunziker, J. C., Desmons, J., & Hurford, A. J. (1992). Thirty-two years of geochronological work in the Central and Western Alps: a review on seven maps. *Mémoires de Géologie (Lausanne), 13*, 1–59.

Inger, S., & Cliff, R. A. (1994). Timing of metamorphism in the Tauern window. *Journal of Metamorphic Geology, 12*, 695–707.

Janots, E., Berger, A., & Engi, M. (2011). Physico-chemical control on the REE minerals in chloritoid-grade metasediments from a single outcrop (Central Alps, Switzerland). *Lithos, 11*, 1–11.

Janots, E., Berger, A., Gnos, E., Whitehouse, M. J., Lewin, E., & Pettke, T. (2012). Constraints on fluid evolution during metamorphism from U–Th–Pb systematics in Alpine hydrothermal monazite. *Chemical Geology, 326*(327), 61–71.

Janots, E., Negro, F., Brunet, F., Goffé, B., Engi, M., & Bouybaouène, M. L. (2006). Evolution of the REE mineralogy in HP–LT metapelites of the Sebtide complex, Rif, Morocco: monazite stability and geochronology. *Lithos, 87*, 214–234.

Kirkland, C. L., Whitehouse, M. J., & Slagstad, T. (2009). Fluid-assisted zircon and monazite growth within a shear zone: a case

study from Finnmark, Arctic Norway. *Contributions to Mineralogy and Petrology, 158*, 637–657.

Krenn, K., Kurz, W., Fritz, H., & Hoinkes, G. (2011a). Eoalpine tectonics of the Eastern Alps: implications from the evolution of monometamorphic Austroalpine units (Schneeberg and Radenthein Complex). *Swiss Journal of Geosciences, 104*, 471–491.

Krenn, K., Putz, H., Finger, F., & Paar, W. H. (2011b). Sulfur-rich monazite with high common Pb in ore-bearing schists from the Schellgaden mining district (Tauern Window, Eastern Alps). *Mineralogy and Petrology, 102*, 51–62.

Lambert, R. S. J. (1970). A potassium-argons study of the margin of the Tauern widow at Döllach, Austria. *Eclogae Geologicae Helveticae, 63*, 197–205.

Liang, J. L., Sun, W. D., Li, Y. L., Zhu, S. Y., Li, H., Liu, Y. L., & Zhai, W. (2013). An XPS study on the valence states of arsenic in arsenian pyrite: implications for Au deposition mechanism of the Yang-shan Carlin-type gold deposit, western Qinling belt. *Journal of Asian Earth Sciences, 62*, 363–372.

Liu, Y., Hu, Z., Gao, S., Günther, D., Xu, J., Gao, C., & Chen, H. (2008). In situ analysis of major and trace elements of anhydrous minerals by LA-ICP-MS without applying an internal standard. *Chemical Geology, 257*, 34–43.

Luckscheiter, B., & Morteani, G. (1980). Microthermometrical and chemical studies on fluid inclusions in minerals from Alpine veins from the Penninic rocks of the central and western Tauern window (Austria/Italy). *Lithos, 13*, 61–77.

Ludwig, K. R. (2001). *Isoplot 3.0-A geochronological toolkit for Microsoft Excel*. 1–71 p, Berkeley, California.

Luth, S. W., & Willingshofer, E. (2008). Mapping of the post-collisional cooling history of the Eastern Alps. *Swiss Journal of Geoscience, 101*(Supplement), S207–S223.

Mannucci, G., Diella, V., Gramaccioli, C. M., & Pilati, T. (1986). A comparative study of some pegmatitic and fissure monazite from the Alps. *The Canadian Mineralogist, 24*, 469–474.

McDonough, W. F., & Sun, S. S. (1995). The composition of the Earth. *Chemical Geology, 120*, 223–253.

Meldrum, A., Boatner, L. A., & Ewing, R. C. (2000). A comparison of radiation effects in crystalline ABO(4)-type phosphates and silicates. *Mineralogical Magazine, 64*, 185–194.

Meldrum, A., Boatner, L. A., Wang, S. J., Wang, S. X., & Ewing, R. C. (1999). Effects of dose rate and temperature on the crystalline-to-metamict transformation in the ABO(4) orthosilicates. *Canadian Mineralogist, 37*, 207–221.

Meldrum, A., Boatner, L. A., Weber, W. J., & Ewing, R. C. (1998). Radiation damage in zircon and monazite. *Geochimica and Cosmochimica Acta, 62*, 2509–2520.

Montel, J. M., Foret, S., Veschambre, M., Nicollet, C., & Provost, A. (1996). Electron microprobe dating of monazite. *Chemical Geology, 131*, 37–53.

Montel, J. M., Veschambre, M., & Nicollet, C. (1994). Dating Monazite with the electron microprobe. *Comptes Rendus de l'Académie des Sciences, Série II, 318*, 1489–1495.

Mullis, J. (1996). P-T-t path of quartz formation in extensional veins of the Central Alps. *Schweizerische Mineralogische und Petrographische Mitteilungen, 76*, 159–164.

Mullis, J., Dubessy, J., Poty, B., & O'Neil, J. (1994). Fluid regimes during late stages of a continental collision: physical, chemical, and stable isotope measurements of fluid inclusions in fissure quartz from a geotraverse through the Central Alps, Switzerland. *Geochimica et Cosmochimica Acta, 58*, 2239–2267.

Nasdala, L., Finger, F., & Kinny, P. (1999). Can monazite become metamict? *European Journal of Mineralogy, 11*, 164.

Niedermayr, G. (1980). Ostalpine Kluftmineralisationen und ihre Beziehungen zur alpidischen Metamorphose. *Annalen des Naturhistorischen Museumsin Wien, 83*, 399–416.

Niedermayr, G., Auer, C., Bernhard, F., Blass, G., Hirche, T., Huber, P. A., et al. (2010). Neue Mineralienfunde aus Oesterreich LIX. *Carintihia, 200*, 230–231.

Niggli, P., Königsberger, J., Parker, R. L. (1940). *Die Mineralien der Schweizeralpen* (661 pp.). Basel, B. Wepf & Co.

Ondrejka, M., Uher, P., Pršek, J., & Ozdín, D. (2007). Arsenian monazite-(Ce) and xenotime-(Y), REE arsenates and carbonates from the Tisovec-Rejkovo rhyolite, Western Carpathians, Slovakia: composition and substitutions in the (REE,Y)XO4 system (X = P, As, Si, Nb, S). *Lithos, 95*, 116–129.

Parrish, R. R. (1990). U-Pb dating of monazite and application to geological problems. *Canadian Journal of Earth Sciences, 27*, 1431–1450.

Pestal, G., Hejl, E., Braunstingl, R., & Schuster, R. (2009). *Erläuterungen zur geologischen Karte von Salzburg 1: 200 000* (pp. 1–162). Wien: Geologische Bundesanstalt.

Pettke, T., Oberli, F., Audetat, A., Guillong, M., Simon, A. C., Hanley, J. J., & Klemm, L. M. (2012). Recent developments in element concentration and isotope ratio analysis of individual fluid inclusions by laser ablation single and multiple collector ICP-MS. *Ore Geology Reviews, 44*, 10–38.

Purdy, J. W., & Stalder, H. A. (1973). K-Ar ages of fissure minerals from the Swiss Alps. *Schweizerische Mineralogische und Petrographische Mitteilungen, 53*, 79–98.

Ratschbacher, L., Frisch, W., Linzer, H.-G., & Merle, O. (1991). Lateral extrusion in the eastern Alps, Part 2: structural analysis. *Tectonics, 10*, 257–271.

Reddy, S. M., Cliff, R. A., & East, P. (1993). Thermal history of the Sonnblick Dome, southeast Tauern Window, Austria: implications for heterogeneous uplift within the Penninic basement. *Geologische Rundschau, 82*, 667–675.

Reiners, P.W. (2005). Zircon (U-Th)/He thermochronology. In: P. W. Reiners, T. A. Ehlers (Eds.), *Low-temperature thermochronology* (pp.151–176). Chantilly, Virginia, Mineralogical Society of America, 58.

Rosenberg, C. L., Berger, A. (2009). On the causes and modes of exhumation and lateral growth of the Alps, Tectonics, 28, TC6001, doi:10.1029/2008TC002442.

Scharf, A., Handy, M. R., Ziemann, M. A., & Schmid, S. M. (2013). Peak-temperature patterns of polyphase metamorphism resulting from accretion, subduction and collision (eastern Tauern Window, European Alps) - a study with Raman micropectrometry on carbonaceous material (RSCM). *Journal of Metamorphic Geology, 31*, 863–880.

Scherrer, N. C., Engi, M., Gnos, E., Jakob, V., & Liechti, A. (2000). Monazite analysis from sample preparation to microprobe age dating and REE quantification. *Schweizerische Mineralogische und Petrographische Mitteilungen, 80*, 93–105.

Schmid, S., Fügenschuh, B., Kissling, E., & Schuster, R. (2004). The tectonic map and overall architecture of the Alpine orogen. *Eclogae Geologicae Helveticae, 97*, 93–117.

Schmid, S., Scharf, A., Handy, M. R., & Rosenberg, C. I. (2013). The Tauern Window (Eastern Alps, Austria): a new tectonic map, with cross-sections and tectonometamorphic synthesis. *Swiss Journal of Geosciences, 106*, 1–32.

Schulz, B., & von Raumer, J. F. (2011). Discovery of Ordovician-Silurian metamorphic monazite in garnet metapelites of the Alpine External Aiguilles Rouges Massif. *Swiss Journal of Geosciences, 104*, 67–79.

Seydoux-Guillaume, A. M., Montel, J.-M., Bingen, B., Bosse, V., de Parseval, P., Paquette, J.-L., et al. (2012). Low-temperature alteration of monazite: fluid mediated coupled dissolution-precipitation, irradiation damage, and disturbance of the U-Pb and Th-Pb chronometers. *Chemical Geology, 330–331*, 140–158.

Seydoux-Guillaume, A. M., Paquette, J. L., Wiedenbeck, M., Montel, J. M., & Heinrich, W. (2002). Experimental resetting of the U-Th-Pb system in monazite. *Chemical Geology, 191*, 165–181.

Stacey, J. S., & Kramer, J. D. (1975). Approximation of terrestrial lead isotope evolution by a 2-stage model. *Earth and Planetary Science Letters, 26*, 207–222.

Staufenberg, H. (1987). Apatite fisson-track evidence for postmetamorphic uplift and cooling history of the Tauern Window and the surrounding Austroalpine (Central Eastern Alps, Austria). *Jahrbuch der Geologischen Bundesanstalt, 130*, 571–586.

Steiger, R. H., Jäger, E., & Subcomission of geochronology. (1977). Convention of the use of decay constants in geo- and cosmochronology. *Earth and Planetary Science Letters, 36*, 359–362.

Steininger, R. R., Berggren, W. A., Kent, D. V., Bernor, R. L., Sen, S., Agusti, J. (1996). Circum Mediterranean Neogene (Miocene and Pliocene). Marine-Continental chronologic correlations of European mammal units and zones. In: R. L. Bernor, V. Fahlbusch, S. Rietschel (Eds.) *Later Neogene European Biotic Evolution and Stratigraphic Correlation* (pp. 7–46). New York: Columbia University Press.

Suzuki, K., & Adachi, M. (1991). Precambrian provenance and Silurian metamorphism of the Tsubonosawa paragenesis in the South Kitakami terrane, Northeast Japan, revealed by chemical Th-U-total Pb isochron ages of monazite, zircon, and xenotime. *Geochemical Journal, 25*, 641–648.

Suzuki, K., Adachi, M., & Kajizuka, I. (1994). Electron microprobe observations of Pb diffusion in metamorphosed detrital monazites. *Earth and Planetary Science Letters, 128*, 391–405.

Thöni, M. (1999). A review of geochronological data from the Eastern Alps. *Schweizerische Mineralogische und Petrographische Mitteilungen, 79*, 209–230.

Todd, C. S., & Engi, M. (1997). Metamorphic field gradients in the central Alps. *Journal of Metamorphic Geology, 15*, 513–530.

von Blanckenburg, F., Villa, I. M., Baur, H., Morteani, G., & Steiger, R. H. (1989). Time calibration of a PT-path from the western Tauern Window. *Contributions to Mineralogy and Petrology, 101*, 1–11.

Waters, D. J. (1976). *Structural, metamorphic and geochronological studies in the south east Tauern Window*. Oxford: Unpublished PhD thesis, University of Oxford.

Weiss, S., Duthaler, R., & Praeger, M. (2005). Von 1881 bis 2003: Die Euklasfunde der Alpen. Teil 1: Fundstellen in Österreich, Oberitalien und der Südschweiz. *Lapis, 2004/9*, 23–34.

Williams, M. L., Jercinovic, M. J., Harlov, D. E., Budzyn, B., & Hetherington, C. J. (2011). Resetting monazite ages during fluid-related alteration. *Chemical Geology, 283*, 218–225.

Wölfler, A. (2008). *Tectonothermal evolution of the southeastern Tauern Window and the adjacent austroalpine basement of the Kreuzberg Massif: evidence from combined fission track and (U-Th)/He analyses* (p. 80). Tübingen: PhD-thesis, Universität Tübingen.

Wölfler, A., Stüwe, K., Danisik, M., & Evans, J. E. (2012). Low temperature thermochronology in the Eastern Alps: implications for structural and topographic evolution. *Tectonophysics, 541–543*, 1–18.

Yamada, R., Tagami, T., Nishimura, S., & Ito, H. (1995). Annealing kinetics of fission tracks in zircon: an experimental study. *Chemical Geology, 122*, 249–258.